

ARMY RESEARCH LABORATORY



Ground Viewing Perspective Hyperspectral Anomaly Detection

by Dalton Rosario and Joao Romano

ARL-TR-4583

September 2008

NOTICES

Disclaimers

The findings in this report are not to be construed as an official Department of the Army position unless so designated by other authorized documents.

Citation of manufacturer's or trade names does not constitute an official endorsement or approval of the use thereof.

Destroy this report when it is no longer needed. Do not return it to the originator.

Army Research Laboratory

Adelphi, MD 20783-1197

ARL-TR-4583

September 2008

Ground Viewing Perspective Hyperspectral Anomaly Detection

Dalton Rosario

Sensors and Electron Devices Directorate, ARL

and

Joao Romano

Army Armament Research, Development, and Engineering Center

REPORT DOCUMENTATION PAGE				Form Approved OMB No. 0704-0188	
<p>Public reporting burden for this collection of information is estimated to average 1 hour per response, including the time for reviewing instructions, searching existing data sources, gathering and maintaining the data needed, and completing and reviewing the collection information. Send comments regarding this burden estimate or any other aspect of this collection of information, including suggestions for reducing the burden, to Department of Defense, Washington Headquarters Services, Directorate for Information Operations and Reports (0704-0188), 1215 Jefferson Davis Highway, Suite 1204, Arlington, VA 22202-4302. Respondents should be aware that notwithstanding any other provision of law, no person shall be subject to any penalty for failing to comply with a collection of information if it does not display a currently valid OMB control number.</p>					
PLEASE DO NOT RETURN YOUR FORM TO THE ABOVE ADDRESS.					
1. REPORT DATE (DD-MM-YYYY)	2. REPORT TYPE		3. DATES COVERED (From - To)		
September 2008	Final		FY08		
4. TITLE AND SUBTITLE			5a. CONTRACT NUMBER		
Ground Viewing Perspective Hyperspectral Anomaly Detection			5b. GRANT NUMBER		
			5c. PROGRAM ELEMENT NUMBER		
			5d. PROJECT NUMBER		
6. AUTHOR(S)			5e. TASK NUMBER		
Dalton Rosario (ARL) and Joao Romano (ARDEC)			5f. WORK UNIT NUMBER		
7. PERFORMING ORGANIZATION NAME(S) AND ADDRESS(ES)			8. PERFORMING ORGANIZATION REPORT NUMBER		
U.S. Army Research Laboratory ATTN: AMSRD-ARL-SE-SE 2800 Powder Mill Road Adelphi, MD 20783-1197			ARL-TR-4583		
9. SPONSORING/MONITORING AGENCY NAME(S) AND ADDRESS(ES)			10. SPONSOR/MONITOR'S ACRONYM(S)		
Army Armament Research, Development, & Engineering Center Picatinny Arsenal NJ 07806-5000			11. SPONSOR/MONITOR'S REPORT NUMBER(S)		
12. DISTRIBUTION/AVAILABILITY STATEMENT Approved for public release; distribution unlimited.					
13. SUPPLEMENTARY NOTES					
14. ABSTRACT <p>The U.S. Army Research Laboratory (ARL) has teamed with the Armament Research, Development and Engineering Center (ARDEC) to develop and demonstrate performance of innovative algorithmic approaches for applications requiring autonomous detection and classification of military targets (e.g., ground vehicles, camouflaged personnel) using passive hyperspectral (HS) devices. This report focuses on the first stage of a two-stage algorithm suite under development and the application of this first stage to the detection of manmade material. The two-stage algorithm suite features autonomous clutter background characterization (ACBC), adaptive anomaly detection, and constrained subspace target classification, where the first stage highlights anomalous structures in the imagery and the second stage classifies these structures as known materials (targets) or unknown materials (targets or non-targets). The first stage has two main components, ACBC and anomaly detection. The uniqueness of this first stage is that a random sampling model is proposed as a parallel process in order to mitigate the likelihood that samples of targets are erroneously used during imagery testing as clutter-background spectral references. This approach is proposed to handle underlying difficulties (target shape/scale uncertainties) often ignored in the development of autonomous anomaly detection algorithms. Experimental results, using no prior information about the clutter background, are presented for the ACBC/anomaly detection approach testing multiple examples of real HS data cubes.</p>					
15. SUBJECT TERMS Hyperspectral data, anomaly detection, ground view					
16. SECURITY CLASSIFICATION OF:			17. LIMITATION OF ABSTRACT	18. NUMBER OF PAGES	19a. NAME OF RESPONSIBLE PERSON
			UU	50	Dalton Rosario
a. REPORT	b. ABSTRACT	c. THIS PAGE			19b. TELEPHONE NUMBER (Include area code) (301) 394-4235
U	U	U			

Contents

List of Figures	iv
Summary	1
1. Introduction	3
1.1 Background	3
1.2 Application of Statistical Models	3
1.3 Statistical Models for HS Data.....	4
1.4 Relevant Work.....	5
1.5 Overview of This Work.....	7
2. Autonomous Sampling of the Cluttered Environment	8
2.1 Description of the SOC-700 Hyperspectral Data.....	9
2.2 A Binomial Based Parallel Random Sampling Model.....	11
3. Ground-View Hyperspectral Anomaly Detection	15
3.1 Multivariate GV Anomaly Detection	15
3.2 Univariate GV Anomaly Detection.....	18
4. Summary of Results	20
4.1 Initial Results.....	21
4.2 Adaptive Threshold Under Various Environment Conditions	26
4.2.1 Description of Additional Data	26
4.2.2 Automatic Parameter Setting.....	29
4.2.3 Adaptive Cutoff Threshold.....	29
5. Conclusion	35
References	36
Acronyms	39
Distribution List	40

List of Figures

Figure 1. Examples of GV imagery. An effective GV anomaly detection algorithm suite would allow a machine to accentuate the presence of targets, while suppressing the cluttered environment, using no prior information about what constitutes clutter background or target in the imagery.	10
Figure 2. N small ($n \times n$) blocks of data are randomly (autonomously) selected from the imagery ($R \times C$) area, as spectral reference sets. In autonomous remote sensing applications, since it is unknown a priori whether target pixels are present in the imagery, a probability $P(m \geq 1)$ exists of at least a block of data being contaminated with target pixels.....	12
Figure 3. The probability $P(m \geq 1)$ of having at least a (1×1) block of data contaminated with a target pixel, as a function of N (the number of randomly selected (1×1) blocks of data), for two given values of q (the probability of randomly selecting a target pixel in the imagery area). These curves are conservative upper bounds, because target pixels are assumed to be randomly distributed across the imagery area, but in practice pixels are clustered per each target.....	13
Figure 4. The probability $\tilde{P}(\tilde{m} = M)$ that all M random sampling processes(repetitions) will have at least a contaminated block of data decreases as a function of increasing M , given that each independent process has a probability $P_g(m \geq 1)$ of being contaminated.....	14
Figure 5. Parallel random sampling approach for GV anomaly detection, where detector's output surfaces are fused by summing pixelwise the surfaces.	17
Figure 6. PRS-AVT results on Cube 1 (top left) for scene anomalies; output surface (top right) using parameters ($q = 0.1$; $N = 3$; $M = 3$); and output surface (bottom left) using parameters ($q = 0.1$; $N = 22$; $M = 40$). Brighter pixels values in the output surfaces correspond to higher confidence on the presence of anomalies in the imagery, relative to randomly selected blocks of data. Also, notice that since \mathbf{Z}_{AVT} is a sum of results, bright clusters in those surfaces are smooth clusters.....	22
Figure 7. PRS-AVT results on Cube 2 (top left) and Cube 3 (bottom left), where corresponding output surfaces are shown immediately to the right of the cube displays. Parameters were set to ($q = 0.1$; $N = 22$; $M = 40$).....	23
Figure 8. PRS-AVT results on Cube 4 (left), and corresponding output surface (right). Parameters were set to ($q = 0.1$; $N = 22$; $M = 40$). Cube 4 exemplifies a hard case for autonomous clutter suppression.....	24
Figure 9. Comparison results for PRS-AVT and PRS-RX on Cube 3 (bottom center) by setting N to three different values (10, 50, and 100); the corresponding PRS-RX output surfaces are shown in the left column, and the corresponding PRS-AVT output surfaces are shown in the right column.....	25
Figure 10. A target site under different environmental conditions.....	28

Figure 11. PRS-AVT thresholded fused-output surface (top right) using parameters ($q = 0.1$; $N = 22$; $M = 40$) and $T(10)$; Overlaid results using threshold $T(10)$ (bottom right) and $T(30)$ (bottom left). At 30 sigma, both targets are fully detected with no false positives. Because of the targets' different angular orientations, they appear to have different scales and shapes.....	31
Figure 12. PRS-AVT overlaid results for Lower Fog, using parameters ($q = 0.1$; $N = 22$; $M =$ 40) and adaptive thresholds $T(5)$, $T(10)$, $T(20)$, $T(30)$, and $T(50)$	32
Figure 13. PRS-AVT overlaid results, using parameters ($q = 0.1$; $N = 22$; $M = 40$) and adaptive threshold $T(30)$. In all cases, PRS-AVT yielded virtually zero false alarms detecting both targets.	34

INTENTIONALLY LEFT BLANK.

Summary

The objective of this work is to propose and evaluate specific algorithms using—as input—transformed hyperspectral (HS) data in order to obtain novel forms for output surfaces, and then use these output surfaces to improve the performance of candidate ground view (GV) anomaly detection systems.

To date, a significant amount of research has focused on classification and detection algorithms using parametric HS data models as foundation for algorithm development, while little has been done to address the underlying fundamental problems that affect algorithm performances. One goal of this work is to identify a short list of fundamental performance challenges for existing local and global anomaly detection algorithms, and then use this list to find from a large population of scoring algorithms those metrics that could perform more robustly over these fundamental challenges. Another goal is to introduce to the HS research community the state of the art in global anomaly detection, which does not require segmentation of the HS image data. Global anomaly detection often requires segmentation in the prior art.

This report identifies three underlying key factors in spectra—spectral magnitude, spectral shape, and spectral mixture—that can interfere with detection performance, as observed through sliding small windows.

A data transformation method is introduced to reduce algorithm sensitivity to spectral magnitude, while preserving high sensitivity to spectral shape; both properties are desired for effective anomaly detection. In addition, an asymmetric scoring metric is introduced to handle spectral mixtures, where each scoring metric uses two transformed spectral samples.

Finally, this report presents a fully operational GV global anomaly detection algorithm and evaluates the approach using real HS data cubes, where some targets are present in a natural clutter background under different illumination and atmospheric conditions. The uniqueness of this GV anomaly detection approach is that a random sampling model is proposed as a parallel process in order to mitigate the likelihood that samples of targets are erroneously used as clutter spectral references during imagery testing. The cumulative probability \tilde{P} of taking target samples by chance during parallel processing were modeled by the binomial distribution family, such that $\tilde{P} = [1 - (1 - q)^N]^M$, where N is the number of randomly selected $n \times n$ blocks of data, taken from data cube \mathbf{X} (per repetition or process), M is the number of parallel processes, and q (the only target related parameter) is a proportion (an upper bound guess) of the maximum total number a of all target pixels over the total number of pixels (RC) in \mathbf{X} , i.e., $\left(q = \frac{a}{RC} \right)$. Note that q is invariant to target scale, target shape, or to the number of targets in \mathbf{X} . For instance, $q = 0.05$ indicates that targets in the imagery area are not expected to cover more than 5% of the entire

image area in \mathbf{X} . Choosing a sensible q for the given application, one can use $\tilde{P} = [1 - (1 - q)^N]^M$ to assist on tradeoff decisions between N and M for a desired (small) \tilde{P} [e.g., $\tilde{P} = 0.01$].

Moreover, this report shows how N and M can be automatically set using a simple guideline, and how to implement an adaptive cutoff threshold method for the GV global anomaly detection algorithm suite.

Experimental results, using no prior information about the clutter background, are presented from having the GV global anomaly detection approach testing multiple examples of real HS data cubes, showing favorable outcomes.

1. Introduction

1.1 Background

The field of spectroscopy examines the electromagnetic radiation that each unique material reflects, absorbs, and emits. The electromagnetic spectrum is sampled at a sufficiently large number of spectral bands to create a discrete spectral signature for different materials. In theory, each spectral signature should be unique for each unique material owing to its molecular structure. The ability to identify, within certain limits, physical materials from their spectral signature is the basis behind remote sensing imaging spectroscopy (1).

Remote sensing imaging spectroscopy involves using an airborne or space-borne platform with a sensor that records the reflected or emitted electromagnetic radiation. The sensor collects the radiation over a wide range of contiguous spectral bands, with each band corresponding to a unique spectral value. As the sensor moves above a region it records the electromagnetic radiation from a narrow swath of land, in many different spectral channels. The field of view of the sensor is broken into hundreds of thousands of pixels, with each pixel representing from less than one to many squared meters of the region of interest depending on the spatial resolution of the sensor and the height of the sensor during the data collection. A collection of spatial-spectral images is put together resulting in a hyperspectral (HS) data cube, where the length and width represent the spatial dimension, and the depth represents the spectral dimension (2).

The resulting HS data cube consists of hundreds of thousands of pixels. Each pixel has tens or hundreds of data points, each point corresponding to a unique spectral value. In theory, the spectral signature of each pixel should uniquely characterize the physical material in that spatial land area. In practice, the recorded spectral signatures will never be identical for samples of the same material. Owing to the different illumination conditions, atmospheric effects, sensor noise, etc., the resulting spectral signatures for HS data pixels containing similar materials will exhibit spectral variability.

1.2 Application of Statistical Models

Each spectral signature can be represented by a multidimensional vector, where each vector dimension represents a different spectral band. The spectrum of each pixel in a HS data cube is a vector lying in a multidimensional space. All pixels containing the same material and roughly the same amount of illumination will have their vector spectra closely grouped within the vector space, forming a sort of data cloud in the multidimensional space. The overall data space may contain many different homogeneous data clouds corresponding to the different materials in the HS data cube. Provided there are enough pixels in the data cube, or sample, this spectral variability can be modeled as a multivariate probability distribution.

Accurate models for the spectral variability of HS data are useful in many applications. Indeed, these models can be used to develop and evaluate algorithms for classification and detection, select proper thresholds, and generate synthetic data.

Classification algorithms use probability distribution models to group the pixels of like material into spectrally homogeneous data sets. Classification algorithms label each pixel in such a way that similar material pixels have the same label and the data can be segmented into spectrally homogeneous clusters. The material of each cluster can then be determined using available ground truth or comparing the statistical nature of the clustered pixels to that of a library of known materials.

Classification of HS image data has many applications. The classification labels can be used to determine the number of pixels of a particular material type in a scene, and since each pixel covers a spatial region, it is related to the amount of a material present. In commercial applications, this could be used, for instance, to compute farming yields, where the number of pixels of a specific crop could be used to estimate the amount of crop to be produced.

Detection algorithms use the probability distribution models to find pixels which contain a specific material of interest (target). The target pixels are considered rare relative to the number of pixels, which do not contain the target. Otherwise classification algorithms are used to segment the pixels. When the exact target signature is not known a priori, then the probabilistic models can be used to find pixels which are spectrally anomalous. In applications of anomaly detection algorithms, one tries to find objects that are significantly different spectrally from the other pixels within a scene.

Probabilistic models are also useful for generating synthetic HS data. The resulting synthetic data would have the same spectral variability as real world data and can be used to evaluate the classification and detection algorithms under different conditions.

Classification and detection applications require accurate statistical models of the HS data to be effective. Without accurate models, the algorithms' performance is significantly reduced.

1.3 Statistical Models for HS Data

Statistical signal processing uses a finite number of samples to model the probability of the data. The multivariate model defines the probability density function of the data. The effectiveness of a data model depends upon how accurately it represents all aspects of the data and how widely it applies.

Most utilized models are parametric, where the shape of a particular model is controlled by a set of parameters. If all of the parameters are known a priori, then the data model is completely known. When the parameters are not known a priori, they need to be estimated from the available data set.

For HS data, where the model and model parameters are not known a priori, typically a model for the spectral variability of the pixels is proposed and the model parameters are estimated using an entire HS dataset. The goal is to model the multivariate spectral variability of a particular dataset as accurately as possible, where each pixel $\mathbf{x}_{rc} \in \mathbf{R}^K$ ($1 \leq r \leq R; 1 \leq c \leq C$) has K spectral bands, and the complete data cube $\mathbf{X} \in \mathbf{R}^{R \times C \times K}$ consists of RC pixels. The objective of statistical modeling of HS data is to propose a spectral probability distribution model and estimate its parameters:

$$\text{Given Multivariate Data: } \mathbf{X} = \begin{bmatrix} \mathbf{x}_{11}, \mathbf{x}_{12}, \dots, \mathbf{x}_{1C} \\ \mathbf{x}_{21}, \mathbf{x}_{22}, \dots, \mathbf{x}_{2C} \\ \vdots \\ \mathbf{x}_{R1}, \mathbf{x}_{R2}, \dots, \mathbf{x}_{RC} \end{bmatrix}$$

$$\text{Proposed Multivariate Model: } \mathbf{x}_{rc} \sim f_K(\mathbf{x}; \Theta)$$

$$\text{Estimate Model Parameters: } \hat{\Theta}$$

Since it is not possible to know the exact distribution of the data, real world processing of HS data must rely on limited information. The accuracy of the model parameter estimates depends on the number of HS data vectors. Due to the variation in spectral illumination, the different types of material present during each data collection, and other factors, only data collected during a single collection can be used to estimate the parameters of the multivariate model. In other words, the models must be determined in an adaptive manner from the HS data directly, with each HS dataset having different model parameters (3).

The primary model used for the spectral variability of HS image data is the multivariate normal distribution. While this model might do an adequate job modeling the main body of the data, rarely does it do an adequate job in modeling the tails of the distributions (3, 4). For detection applications at a low probability of false alarms, with hundreds of thousands pixels in a HS data cube, incorrectly classifying a few hundred pixels might not have a large effect on the overall classification of a scene. However, if, for example, a detection threshold is set with the expectation of one or two false alarms in the scene, and hundreds of pixels score higher than the threshold and are incorrectly labeled as targets, then the results of the detection algorithm become unreliable and of little value.

1.4 Relevant Work

In practice, it has been observed (5) that finding accurate models for high dimensional HS data may be unrealistic. Implementation of a parametric classifier for HS data is often cumbersome, it requires an unreasonably large set of training data to adequately characterize the multidimensional probability surface of each scene or target set, and it is difficult to store the

description of such a surface unless it is well behaved (5). It has also been observed (6) that it is extremely difficult to obtain an accurate density estimate nonparametrically in high-dimensional spaces. For these reasons, general class-conditional distribution functions are often replaced by a more tractable class-conditional distribution function for classification or detection using HS data.

Examples of parametric multivariate-normal-based target detection algorithms are the matched filter (7), the kernel spectral matched filter (8), and linear mixture models (9–11). Another main limitation of these representative parametric algorithms, in addition to assuming normality for HS data, is that they require a known target signature, and reliable target signatures are difficult to ascertain due to spectral variations already discussed in section 1.1.

An alternative approach that does not require a spectral library for targets and has potential for invariance to atmospheric and illumination effects is anomaly detection, global or local.

Existing global anomaly detectors require that the HS data cube is first segmented into its constituent material classes. Then detection is achieved by applying a cutoff threshold and automatically locating pixel clusters with pixel values above the threshold, representing the outliers of these classes. These hybrid algorithms vary in the method of segmentation, but tend to use maximum likelihood detection under the multivariate normal distribution. Furthermore, since the correct number of material classes in the scene is unknown *a priori* and needed by segmentation algorithms, this number is an unknown parameter that significantly affects the output results of such algorithms. The stochastic expectation maximization clustering algorithm (12) is a related example, see also reference 13.

Existing local anomaly detectors process small ($n \times n$) windows of the HS data, where data sampling is not done in \mathbf{X} (see subsection 1.3); all the \mathbf{x}_{rc} ($r = 1, \dots, R; c = 1, \dots, C$) in \mathbf{X} are used; modeling is only done at the level of the $n \times n$ windows, where $n \ll R$ and $n \ll C$ (\ll denoting *many orders of magnitude smaller than*); and at the level of the pixel area surrounding these windows. Blocks of data ($n \times n$ windows) that are spectrally different from pixels surrounding them score high using an effective detector in contrast to blocks of data that are not spectrally different from their surrounding pixels. After the detector scores the entire \mathbf{X} , it yields a 2-dimensional (2-dim) surface Z [a $(R-n-1) \times (C-n-1)$ array of scalars], where a cutoff threshold is then compared to the pixel values in Z . Pixels having values greater than the threshold are labeled local anomalies. These are all features of existing anomaly detectors.

The most popular local anomaly detector in the HS research community is based on a maximum likelihood estimation under the multivariate normal distribution; this detector is commonly known as the Reed-Xiaoli (RX) algorithm (14). A *kernelized* version of RX has been also proposed (15). For nonparametric local anomaly detection, the most prominent multivariate detectors use classic methods, such as, Fisher's linear discriminant (15) and principal component decomposition (16, 17).

Because local anomaly detectors (parametric or nonparametric) process small windows across the spatial area of \mathbf{X} , these algorithms are vulnerable to transitions across distinct regions in \mathbf{X} . Region transition events occur once a block of data representing a specific material is compared to a surrounding mixture of pixels representing the same material and one or more additional, but distinct, material types. This sort of events can augment the probability of false alarms in \mathbf{X} because a spectral sample consisting of pixels of two or more material types is, indeed, different from a spectral sample consisting of pixels of a single material. Since existing local anomaly detectors do not directly account for local transitions of distinct regions, there is a need to address the problem.

Finally, local anomaly detectors are limited to applications where the scales of targets in \mathbf{X} (relative sizes of targets to other objects in the imagery) are expected to be known a priori. This prior knowledge is available in air-to-ground (top view) detection applications, where the sensors look straight down at the ground at a known altitude. However, this prior knowledge is not available in ground-to-ground (ground view (GV)) detection applications, where target scales are dependent on the range between sensors and targets. If the goal is to detect targets as spectral local anomalies in the scene, one has to ensure that a small window in the imagery (inside window) is reasonably separated from its surrounding pixel region (outside window) to avoid having a block of target data compared to surrounding pixels that also belong to the same target. So, using the inside-outside window method for sample comparison, properly setting the separation gap between the inside and outside windows must be done a priori and is a critical factor, completely removing GV anomaly detection applications, as candidate applications using inside-outside windows. An alternative sampling method is needed for GV anomaly detection applications.

HS image data offer clear advantages over conventional broadband images—each pixel has K bands in HS image data versus one band in broadband images, but with current detection algorithm vulnerabilities, the topic of robust target detection is still open for research.

1.5 Overview of This Work

This report focuses on the development and evaluation of an algorithm suite for GV anomaly detection applications using HS data cubes. In this context, a target is any manmade object in a natural clutter background, whose spectral signature is not available, and if available, is considered unreliable and is not used in the approach.

An algorithm suite consists of a host of techniques each performing a specific task in order to achieve the overall goal of detecting, autonomously, the presence of targets in the scene as spectral anomalies in the HS imagery, yielding in the process a low false alarm probability.

If targets are present in the scene, each target is assumed to be represented by multiple pixels \mathbf{x}_{rc} ($\mathbf{x}_{rc} \in \mathbf{R}^K; 1 \leq r \leq R; 1 \leq c \leq C$, see subsection 1.3) in data cube \mathbf{X} ($\mathbf{X} \in \mathbf{R}^{R \times C \times K}$), and cover an area in \mathbf{X} greater than or equal to $n \times n$, where $n \ll R$ and $n \ll C$.

This report analyzes \mathbf{X} for GV anomaly detection applications by sliding an $n \times n$ window and proposes to test the observed spectral sample in the $n \times n$ window against N randomly selected $n \times n$ blocks of data taken from \mathbf{X} . This testing approach addresses the uncertainty on target scales, as discussed in subsection 1.4 for local anomaly detectors, by eliminating the need for an outside window. It also automatically addresses the global anomaly detection problem without the need to use unreliable segmentation techniques in \mathbf{X} , as described in subsection 1.4 for global anomaly detectors.

However, as also discussed in subsection 1.4, any testing approach that uses sliding windows is vulnerable to transitions across distinct spectral regions in \mathbf{X} .

This report establishes that using a data transformation method that maps multivariate spectral samples to univariate samples and applying univariate detectors to test the transformed samples can significantly reduce the probability of false alarms in \mathbf{X} compared to multivariate anomaly detectors.

The use of statistical models for the development of detectors described in this work is purely for motivation of particular formulas for calculating *anomaly output surfaces*. In particular, formulas from the RX algorithm (14) and the Asymmetric Variance Test (AVT) algorithm (18) will be utilized in this report.

Using both RX and AVT algorithms, this report presents a fully operational GV anomaly detection algorithm suite and evaluates the suite using real HS data cubes, where targets are present in a natural clutter background under different illumination and atmospheric conditions.

The remainder of this report is organized as follows: section 2 presents our approach to GV anomaly detection, where, subsection 2.1 discusses the Surface Optics Corp. (SOC)-700 HS data used for this experiment, and subsection 2.2 proposes a repeated (parallel) random sampling approach—modeling this approach by a binomial distribution—and discusses how this sampling approach can be implemented in the context of anomaly detection; section 3 summarizes the results using the GV anomaly algorithm to test real GV HS imagery; and section 4 draws some conclusions and suggests follow up work.

2. Autonomous Sampling of the Cluttered Environment

This section addresses the problem of anomaly detection from a ground-to-ground viewing perspective.

If an anomalous object (target) is defined as one made of a material that is spectrally different from all the materials composing its natural clutter background, then the question we attempt to answer in this section is the following: Can an algorithm suite be developed to automatically detect (or accentuate) the presence of targets in a cluttered environment, given that the imagery

was recorded from the ground-to-ground viewing perspective and no prior information is known about the various materials composing the cluttered environment, the number of targets present in the scene (or if targets are present at all), the scales of targets (their relative sizes in the imagery), shapes and material types of these targets, the illumination environment, and atmospheric conditions?

Anomaly detection using GV imagery is significantly harder to address than using TV imagery, because the distances between the sensor and objects in the scene are unavailable for GV imagery, thus, adding one more unknown variable (target scales) to the anomaly detection problem. Note, for instance, that small targets at closer range will look large—and vice versa, and multiple targets in the same scene may have different scales. The sampling method using a fixed dual rectangular window (16) would not be effective in this application because, in the event that target samples are observed in the inside window, it cannot be guaranteed that the samples observed through the outside window will always belong to the clutter background. Therefore, in the event that target samples are simultaneously observed through both inside and outside windows, the detector will likely suppress the pixels representing that window location in the resulting output surface.

To circumvent target scale uncertainties, we propose to automatically take N blocks of data from random locations in the imagery and, since the targets are expected to cover a significantly small area in the imagery, label these data sets as *spectral references* of clutter background. There is, however, a probability that, if targets are present in the scene, some of these spectral reference sets will be *contaminated*, i.e., one of these spectral reference sets includes target pixels. In order to decrease the probability of contamination, we propose to repeat independently this random sampling process M number of times and will show that the probability of taking target samples by chance during these repetitions can be modeled—approximately—by the Binomial distribution family. We will use this approximation to assist on tradeoff decisions.

2.1 Description of the SOC-700 Hyperspectral Data

The GV imagery used for this work was recorded using the SOC-700 visible to near infrared (VNIR) HS spectral imager from Surface Optics Corporation. The system produces HS data cubes of dimensions $R = 640$ by $C = 640$ pixels by $K = 120$ spectral bands between 0.38 and $0.97 \mu\text{m}$. The sensor is commercially available off the shelf (20).

Figure 1 depicts samples of GV imagery recorded with the SOC-700 HS imager; each pixel in any of the four cube examples corresponds to the average of all the band (120) values at that pixel location.

Data cubes Cube 1, Cube 2, and Cube 3 were collected during the month of June 2004 in Fort Hunter Liggett, CA; data cube Cube 4 was collected during the month of April 2008 in Picatinny Arsenal, NJ. From actual ground truth, it is known that the scene in Cube 1 (figure 1) contains three motor vehicles and a standing person in the center of that scene (i.e., two pick-up trucks to the left in proximity to each other, a man slightly forward from the vehicles in the center, and a

sport utility to the right). The cluttered environment in Cube 1, Cube 2, and Cube 3 is dominated by Californian valley-type trees and/or terrain. Cube 2 features the same sport utility vehicle and the same person stand in proximity to each other; they are located in the same valley, but at a different area from the one in Cube 1. Cube 3, although recorded in the same general geo-location of Cube 1 and Cube 2, depicts a significantly more complex scenario, where, from actual ground truth, it is known that a sport utility vehicle is in the shades of a large cluster of trees. Portions of the shadowed vehicle can be observed near the center in Cube 3. Cube 4 was recorded in a wooded region in Picatinny Arsenal, NJ, where (according to the available ground truth) a sport car is located behind several tree trunks and, hence, can be only partially observed in this *heavy* cluttered environment; see figure 1 (left-center in Cube 4).



Figure 1. Examples of GV imagery. An effective GV anomaly detection algorithm suite would allow a machine to accentuate the presence of targets, while suppressing the cluttered environment, using no prior information about what constitutes clutter background or target in the imagery.

The four data cubes in figure 1 are independently displayed as intensity images after linear mapping the gray scale of each to the range 0–255. Pixel intensities shown in each individual surface is only relative to corresponding values in that surface; in other words, pixel values representing the same material (general terrain) may be displayed with different intensities in another surface. This fact explains, for instance, the difference in brightness between the terrains displayed in Cube 2 and Cube 3, given that both the cluttered environment and atmospheric conditions were about the same during collection of both data cubes. The strong reflections from certain parts of the vehicles captured by the sensor in Cube 1 and Cube 2 are not as dominant in Cube 3 because the vehicle in Cube 3 is in tree shades; hence, the terrain in Cube 3 is the strongest reflector in the scene.

2.2 A Binomial Based Parallel Random Sampling Model

A parallel random sampling approach is presented in this subsection for autonomous clutter background characterization (ACBC). Using a favorite detector, this approach is then incorporated into an algorithm suite in order to perform GV anomaly detection. Results from testing this anomaly detection algorithm suite on real GV imagery are also presented in this section.

Assuming that target pixels are present in the $R \times C$ spatial area of a $R \times C \times K$ HS data cube \mathbf{X} (see examples in figure 1), we denote a the total number of target pixels in \mathbf{X} and q the probability of a pixel in \mathbf{X} being a target pixel out of all $A = RC$ pixels in \mathbf{X} , i.e., $q = \frac{a}{A}$. (In most applications q is unknown, and if multiple targets are present in the imagery, a will be the total number of all target pixels included in the imagery; also, these targets may or may not have the same material type.) In order to represent the unknown clutter background in the imagery, let N blocks of data—all having a fixed small area $(n \times n) \ll (R \times C)$ —be randomly selected from the $R \times C$ area (see figure 2). In theory, for $(n \times n) = (1 \times 1)$ and using the assumption that target pixels in \mathbf{X} are disjointed and randomly located across the $R \times C$ imagery area (in practice, this assumption is not satisfied when targets are present in the scene), the probability P that at least one block of data has a target pixel is

$$\begin{aligned} P(m \geq 1) &= p(m=1) + p(m=2) + \cdots + p(m=N) \\ &= 1 - p(m=0), \end{aligned} \quad (1)$$

where p is the binomial density function (23), given parameters q and N , and $m \in \{0, 1, \dots, N\}$ is the number of blocks of data containing a target pixel, or

$$p(m|q, N) = \frac{N!}{m!(N-m)!} q^m (1-q)^{N-m}. \quad (2)$$

(Symbols $|$ and $!$ denote *given parameters* and the *factorial operator*, respectively.)

For convenience, we will refer to $P(m \geq 1)$ as the *probability of contamination* and, consequently, m as the number of *contaminated* blocks of data.

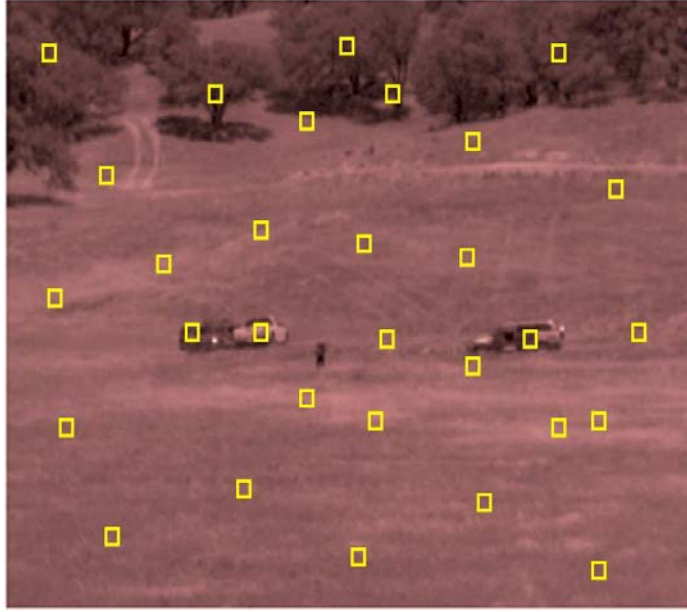


Figure 2. N small ($n \times n$) blocks of data are randomly (autonomously) selected from the imagery ($R \times C$) area, as spectral reference sets. In autonomous remote sensing applications, since it is unknown a priori whether target pixels are present in the imagery, a probability $P(m \geq 1)$ exists of at least a block of data being contaminated with target pixels.

The implementation of this contamination model to the autonomous background sampling problem requires that each one of the N ($n \times n$) blocks of data be regarded as an independent reference set $\mathbf{W}_2^{(f)}$ ($f = 1, 2, \dots, N$) representing clutter spectra, where $\mathbf{W}_2^{(f)} \in \mathbf{R}^{K \times n_2}$ is a rearranged sequence version of the f^{th} block of data having $n_2 = n^2$ spectra. By necessity, n_2 must be significantly greater than 1—for statistical purposes—but yet significantly smaller than $A = R C$ (e.g., $\frac{n_2}{A} = \frac{20^2}{640^2} = 0.000977$) in order to be reasonable to regard a $n \times n$ block of data as an unit area on the $R \times C$ imagery area. A contaminated block of data, then, will be treated qualitatively as a block having target pixels covering a large portion of the block's area (e.g., greater than 0.70). In addition—when targets are present, since pixels representing a single target are expected to be clustered in the imagery, the assumption that each target pixel is randomly located across the imagery area will be ignored. Using equation 1, while ignoring the non-clustered target pixel assumption, implies that the probability of contamination will be overestimated, as blocks of data are less likely to be randomly selected from the same cluster of target pixels. (For the autonomous background sampling problem, it is more conservative to overestimate the probability of contamination than to underestimate.)

Figure 3 shows a plot of the probability of contamination $P(m \geq 1)$ versus N , for two values of q (0.1 and 0.2). It is highlighted in figure 3 that, for instance, if parameters are set to $(q, N) = (0.10, 22)$ then $P(m \geq 1) = 0.90$. Notice that for $N = 22$, if target pixels are present but cover less than $q = 0.10$ of the imagery area, $P(m \geq 1) = 0.90$ is overestimated by two fronts: (1) pixels from a single target are not randomly spread across the imagery area, but clustered, and (2) the cumulative number of target pixels covers less than 0.10 of the imagery area. So, equation 1 provides an upper bound approximation of the probability of contamination, given parameters q and N .

Figure 3 also shows the tradeoff between having a larger number of spectral sets (increasing N) in order to adequately represent the clutter background, which is desired, and the cost of increasing probability of contamination, which is not desired. (More directly, contamination implies that once target pixels are randomly selected by chance from the imagery area, they will be used by a detector as reference set to test the entire imagery, which under the case targets would be suppressed.)

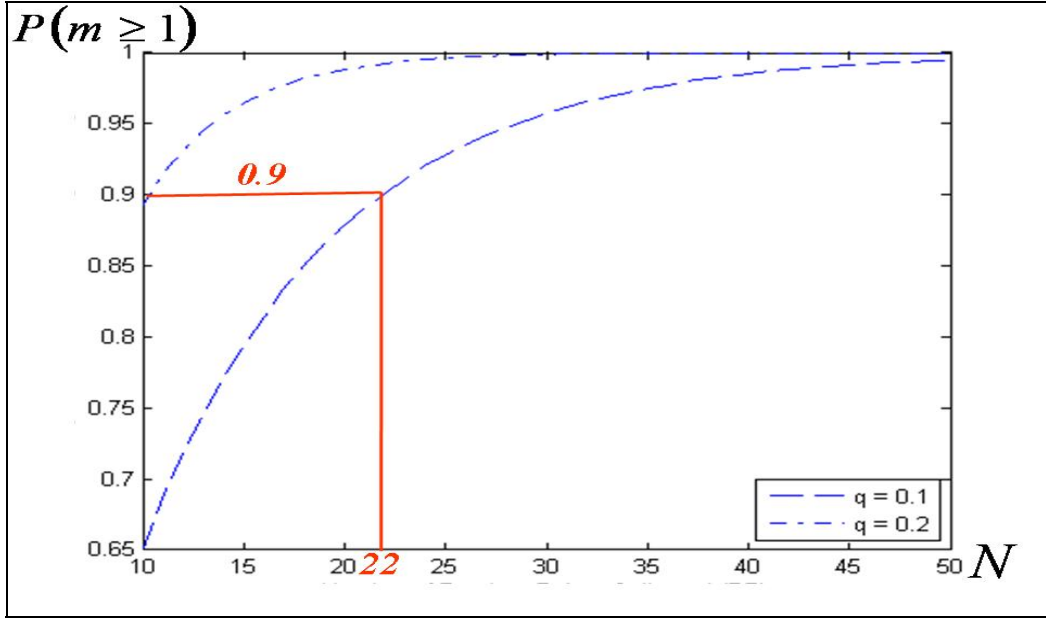


Figure 3. The probability $P(m \geq 1)$ of having at least a (1×1) block of data contaminated with a target pixel, as a function of N (the number of randomly selected (1×1) blocks of data), for two given values of q (the probability of randomly selecting a target pixel in the imagery area). These curves are conservative upper bounds, because target pixels are assumed to be randomly distributed across the imagery area, but in practice pixels are clustered per each target.

Since the presence of target pixels in the imagery is unknown a priori, finding a way to decrease the probability of contamination becomes a necessity. In order to decrease this probability, using an adequately large N and a sensible value for q , we propose to independently repeat the random sampling process described in this subsection M number of times. Figure 4 illustrates the outcome of M repetitions. If we denote the probability of contamination of the g^{th} random

sampling process (or repetition) as $P_g(m \geq 1)$, $1 \leq g \leq M$, for a fixed q and N , note that each $P_g(m \geq 1) = P(m \geq 1)$ and, since $0.0 \leq P(m \geq 1) \leq 1.0$ and these processes will be repeated independently from each other, the overall probability \tilde{P} that *all* the processes will be contaminated with at least a contaminated block of data will decrease as a function of increasing M , or

$$\tilde{P} = P_1(m \geq 1)P_2(m \geq 1)\cdots P_M(m \geq 1) = [P(m \geq 1)]^M. \quad (3)$$

The overall probability of contamination in equation 3 can also be expressed using the binomial distribution by letting \tilde{m} be the number of independent processes that are contaminated out of M repetitions, where $\tilde{m} \in \{0, 1, \dots, M\}$, and using $P(m \geq 1)$ as the probability of contamination per process. It follows that

$$\begin{aligned} \tilde{P}(\tilde{m} = M) &= \frac{M!}{\tilde{m}!(M - \tilde{m})!} [P(m \geq 1)]^{\tilde{m}} [1 - P(m \geq 1)]^{M - \tilde{m}} \\ &= [P(m \geq 1)]^M \\ &= [1 - (1 - q)^N]^M, \end{aligned} \quad . \quad (4)$$

for $N \cdot M \cdot q \ll A$.

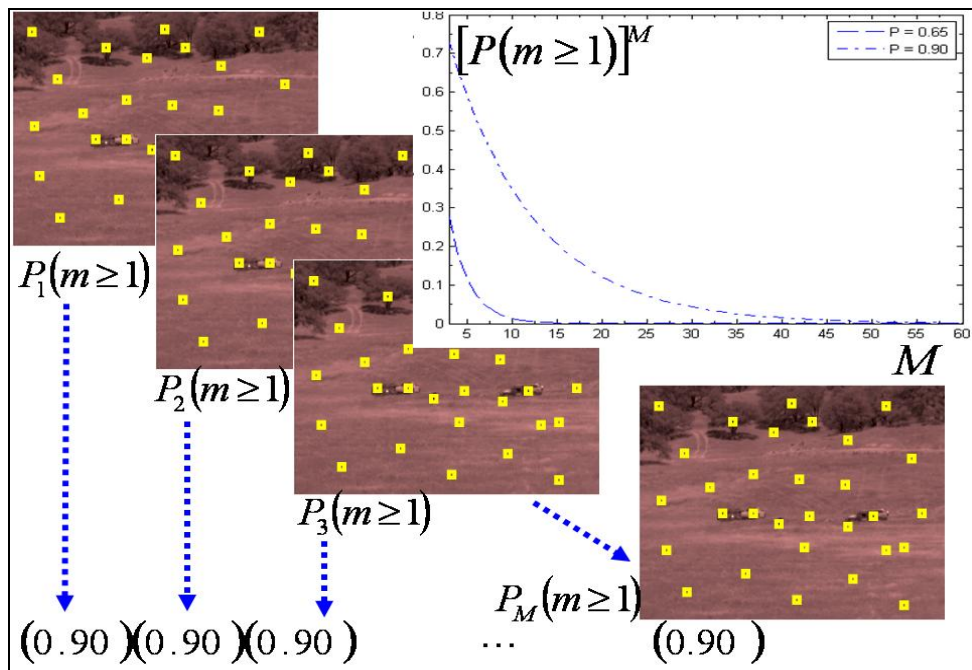


Figure 4. The probability $\tilde{P}(\tilde{m} = M)$ that all M random sampling processes(repetitions) will have at least a contaminated block of data decreases as a function of increasing M , given that each independent process has a probability $P_g(m \geq 1)$ of being contaminated.

Figure 4 also shows a plot of \tilde{P} as a function of increasing M , for $P(m \geq 1) = 0.90$ and $P(m \geq 1) = 0.65$. Taking, as an example, the \tilde{P} curve in figure 4 corresponding to using $P(m \geq 1) = 0.90$ in equation 4, notice that for $M > 40$, $\tilde{P}(\tilde{m} = M)$ decreases to virtually zero. This outcome implies that at least one out of the $M > 40$ processes has an extremely high probability of not being contaminated, as long as $N = 22$ and target pixels do not cover significantly more than 10% of the imagery area ($q = 0.10$). Shortly we will show how to use this autonomous random sampling approach in the context of GV anomaly detection and give some guidelines in how to choose parameters q , N , and M . (Since the M processes are performed independently of each other, this sampling approach will be also called the parallel random sampling approach.)

3. GV Hyperspectral Anomaly Detection

The GV anomaly detection problem can now be addressed using (1) the parallel random sampling approach discussed in subsection 2.2 (needed to characterize the unknown clutter background in the imagery), (2) an effective anomaly detector to test reference data against the entire imagery, (3) a way to fuse the results from testing N randomly chosen blocks of data against the entire imagery using small windows (this will produce a 2-dim output surface per process), and (4) a way to fuse M independently produced 2-dim output surfaces into a single 2-dim decision surface.

We start by choosing a multivariate detector (RX) (14) and a univariate detector (AVT) (18), and follow with a discussion on how to approach (3) and (4) using (1) with these detectors.

3.1 Multivariate GV Anomaly Detection

Let a GV HS data ($R \times C \times K$) cube \mathbf{X} be available for autonomous testing. Let also N blocks ($n \times n$) of data be randomly selected from the \mathbf{X} 's $R \times C$ spatial area and used as a reference library set $\mathbf{W}_2^{(f)}$ ($f = 1, 2, \dots, N$) representing clutter background spectra, where $\mathbf{W}_2^{(f)} = (\mathbf{y}_{21}^{(f)}, \dots, \mathbf{y}_{2n_2}^{(f)})$ is a rearranged sequence version of the f^{th} block of data having $n_2 = n^2$ spectra, where $\{\mathbf{y}_{2u}^{(f)}\}_{u=1}^{n_2} \in \mathbf{R}^K$ are K -dim column vectors. Let $\mathbf{W}_1 = (\mathbf{y}_{11}, \dots, \mathbf{y}_{1n_1})$ be the rearranged version of a ($n \times n$) window of test data at location ij in \mathbf{X} —for column vectors $\{\mathbf{y}_{1h}\}_{h=1}^{n_1} \in \mathbf{R}^K$; first, we would like to automatically test \mathbf{W}_1 against all $\{\mathbf{W}_2^{(f)}\}_{f=1}^N$, and produce a single output (scalar) value $\tilde{Z}_{RX}^{(ij)} \geq 0.0$ from these N test results. Using in this case the RX detector as the base detector, we propose the following:

$$\tilde{Z}_{RX}^{(ij)} = \min_{1 \leq f \leq N} Z_{RX}^{(ij)(f)}, \quad (5)$$

where

$$Z_{RX}^{(ij)(f)} = \frac{n_1 n_2}{n_1 + n_2} \left(\bar{\mathbf{y}}_1 - \bar{\mathbf{y}}_2^{(f)} \right)^t \left(\hat{\Sigma}_2^{(f)} \right)^{-1} \left(\bar{\mathbf{y}}_1 - \bar{\mathbf{y}}_2^{(f)} \right), \quad (6)$$

$$\{Z_{RX}^{(ij)(f)}\}_{f=1}^N \geq 0.0, \quad \bar{\mathbf{y}}_1 = n_1^{-1} \sum_{u=1}^{n_1} \mathbf{y}_{1u}, \quad \bar{\mathbf{y}}_2^{(f)} = n_2^{-1} \sum_{u=1}^{n_2} \mathbf{y}_{2u}^{(f)}, \quad \hat{\Sigma}_2^{(f)} = (n_2 - 1)^{-1} \sum_{u=1}^{n_2} (\mathbf{y}_{2u}^{(f)} - \bar{\mathbf{y}}_2^{(f)}) (\mathbf{y}_{2u}^{(f)} - \bar{\mathbf{y}}_2^{(f)})^t,$$

$n_1 = n_2 = n^2$, and $(i = 1, \dots, R-n-1)$ and $(j = 1, \dots, C-n-1)$ index the left upper corner pixel of an $n \times n$ window in \mathbf{X} .

Notice that if $Z_{RX}^{(ij)(1)}, Z_{RX}^{(ij)(2)}, \dots, Z_{RX}^{(ij)(N)}$ are placed in ascending order and denoted by

$Z_{RX(1)}, Z_{RX(2)}, \dots, Z_{RX(N)}$, such that $Z_{RX(1)} \leq Z_{RX(2)} \leq \dots \leq Z_{RX(N)}$, then $\tilde{Z}_{RX}^{(ij)} = Z_{RX(1)}$ —the lowest order statistics (25).

Notice also that if \mathbf{W}_1 is significantly different from all $\{\mathbf{W}_2^{(f)}\}_{f=1}^N$, then all of the corresponding results $\{Z_{RX}^{(ij)(f)}\}_{f=1}^N$ in equation 6 would yield high values; this outcome means that the lowest order statistics $\tilde{Z}_{RX}^{(ij)}$ in equation 5 would also produce a high value. Otherwise, if \mathbf{W}_1 is significantly similar to at least one of the samples in $\{\mathbf{W}_2^{(f)}\}_{f=1}^N$, then at least one of the corresponding results in $\{Z_{RX}^{(ij)(f)}\}_{f=1}^N$ would yield a low value; this low value would be assigned to $\tilde{Z}_{RX}^{(ij)}$, according to equation 5.

Since it is unknown a priori whether target spectra are present in \mathbf{X} , the entire \mathbf{X} needs to be tested. In order to do it, all $\{\tilde{Z}_{RX}^{(ij)}\}_{i=1, j=1}^{R-n-1, C-n-1}$ must be computed according to equation 5, producing a 2-dim output surface $\tilde{\mathbf{Z}}_{RX}^{(g)}$, or

$$\tilde{\mathbf{Z}}_{RX}^{(g)} = \begin{bmatrix} \tilde{Z}_{RX}^{(11)(g)}, & \tilde{Z}_{RX}^{(12)(g)}, & \dots, & \tilde{Z}_{RX}^{[1(C-n-1)](g)} \\ \tilde{Z}_{RX}^{(21)(g)}, & \tilde{Z}_{RX}^{(22)(g)}, & \dots, & \tilde{Z}_{RX}^{[2(C-n-1)](g)} \\ \vdots & \vdots & \vdots & \vdots \\ \tilde{Z}_{RX}^{[(R-n-1)1](g)}, & \tilde{Z}_{RX}^{[(R-n-1)2](g)}, & \dots, & \tilde{Z}_{RX}^{[(R-n-1)(C-n-1)](g)} \end{bmatrix}, \quad (7)$$

where the index g ($1 \leq g \leq M$) has been introduced to results produced by equation 5 in order to denote the repetition (or process) number discussed in subsection 2.2. (Notice that $\tilde{\mathbf{Z}}_{RX}^{(g)} \in \mathbf{R}^{(R-n-1) \times (C-n-1)}$, which for $n > 1$ is a smaller spatial area than the \mathbf{X} 's $R \times C$ spatial area.)

The result in equation 7 is our approach to (3), as defined in the first paragraph in section 3.

The procedure discussed thus far in this subsection will be independently repeated M number of times, as discussed in subsection 2.2. Using the pixel values $\tilde{Z}_{RX}^{(ij)(g)}$ from $\tilde{\mathbf{Z}}_{RX}^{(g)}$, our approach to

(4), as defined in the first paragraph in section 3, is to sum M results as follows: (the rationale will be explained shortly)

$$\mathbf{Z}_{RX} = \begin{bmatrix} \sum_{g=1}^M \tilde{\mathbf{Z}}_{RX}^{(1)(g)}, & \sum_{g=1}^M \tilde{\mathbf{Z}}_{RX}^{(12)(g)}, & \dots, & \sum_{g=1}^M \tilde{\mathbf{Z}}_{RX}^{[1(C-n-1)](g)} \\ \sum_{g=1}^M \tilde{\mathbf{Z}}_{RX}^{(21)(g)}, & \sum_{g=1}^M \tilde{\mathbf{Z}}_{RX}^{(22)(g)}, & \dots, & \sum_{g=1}^M \tilde{\mathbf{Z}}_{RX}^{[2(C-n-1)](g)} \\ \vdots & \vdots & \vdots & \vdots \\ \sum_{g=1}^M \tilde{\mathbf{Z}}_{RX}^{[(R-n-1)1](g)}, & \sum_{g=1}^M \tilde{\mathbf{Z}}_{RX}^{[(R-n-1)2](g)}, & \dots, & \sum_{g=1}^M \tilde{\mathbf{Z}}_{RX}^{[(R-n-1)(C-n-1)](g)} \end{bmatrix}. \quad (8)$$

Figure 5 illustrates $\tilde{\mathbf{Z}}_{RX}^{(g)}$ equation 7 and \mathbf{Z}_{RX} equation 8 through a parallel random sampling diagram. The diagram shows M independent (parallel) paths, where, in each path, independent blocks of data are randomly selected from the input HS data cube so that the entire data cube can be tested, against these blocks of data, using a testing window of the same block size. Each path, which is indexed by g ($1 \leq g \leq M$), produces a 2-dim output surface $(\tilde{\mathbf{Z}}_{RX}^{(g)})$, where, at the backend of the diagram, all $\{\tilde{\mathbf{Z}}_{RX}^{(g)}\}_{g=1}^M$ are summed *pixelwise* (i.e., only the pixel values at the same pixel location are added), producing a final 2-dim surface \mathbf{Z}_{RX} , as shown in equation 8.

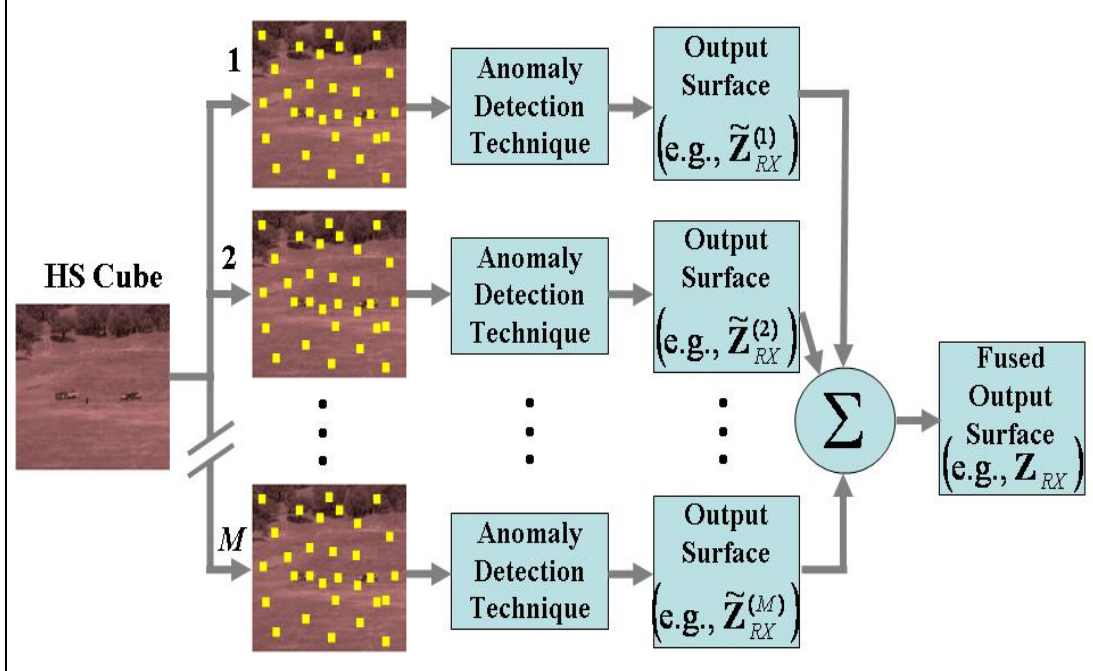


Figure 5. Parallel random sampling approach for GV anomaly detection, where detector's output surfaces are fused by summing pixelwise the surfaces.

For a given repetition g ($1 \leq g \leq M$), we assume that the realization of \mathbf{W}_1 from a window location ij in \mathbf{X} is a spectral sample of a target, and the realizations of $\{\mathbf{W}_2^{(f)}\}_{f=1}^N$ are samples of various materials composing the clutter background in \mathbf{X} , i.e., the randomly selected blocks of data are not contaminated with target spectra. Using an effective anomaly detector, equation 5 is expected to yield a high value for that ij location. Moreover, if the target scale in \mathbf{X} is larger than $n \times n$, then the target will be represented by multiple pixels in $\tilde{\mathbf{Z}}_{RX}^{(g)}$ —see equation 7, having high values. These pixels are expected to be clustered, hence, accentuating the target spatial location in $\tilde{\mathbf{Z}}_{RX}^{(g)}$. However, as discussed in section 2, the contamination probability $P(m \geq 1)$, for a given g , increases as a function of increasing N (see figure 3). Figure 4 shows further that for a fixed q , N and an adequately large M , if (for instance) results $\tilde{Z}_{RX}^{(22)(1)}, \tilde{Z}_{RX}^{(22)(2)}, \dots, \tilde{Z}_{RX}^{(22)(M)}$ correspond to the same portion of the target at testing window location ($i = 2, j = 2$), then equation 4 give us the confidence that at least one term in $\tilde{Z}_{RX}^{(22)(1)}, \tilde{Z}_{RX}^{(22)(2)}, \dots, \tilde{Z}_{RX}^{(22)(M)}$ will have a high value with high probability $[1.0 - \tilde{P}(\tilde{m} = M)]$; we can capture this high value(s) by summing these terms, or for this example $\sum_{g=1}^M \tilde{Z}_{RX}^{(22)(g)}$, as shown in equation 8 for all ij locations. Notice that a target may also be represented by multiple (clustered) pixel locations in \mathbf{Z}_{RX} equation 8.

3.2 Univariate GV Anomaly Detection

The implementation described in subsection 3.1 for the RX detector is readily applicable to other multivariate or univariate detectors, as it is illustrated in this subsection using the univariate based AVT detector.

To use the univariate AVT detector, spectral samples must be first transformed using a transformation method—see reference 18. We can do that by using the N randomly selected blocks of data and arrange to $\mathbf{W}_2^{(f)}$ ($1 \leq f \leq N$), replacing \mathbf{W}_2 in (18) with $\mathbf{W}_2^{(f)}$, and using the index f , accordingly, in the AVT formulas in reference 18, or

$$\begin{aligned} \mathbf{W}_2^{(f)} &= [\mathbf{y}_{21}^{(f)}, \dots, \mathbf{y}_{2n_2}^{(f)}] \\ &= \left[\begin{array}{c} L_{211}^{(f)}, \dots, L_{21n_2}^{(f)} \\ L_{221}^{(f)}, \dots, L_{22n_2}^{(f)} \\ L_{231}^{(f)}, \dots, L_{23n_2}^{(f)} \\ \vdots \\ L_{2(K-2)1}^{(f)}, \dots, L_{2(K-2)n_2}^{(f)} \\ L_{2(K-1)1}^{(f)}, \dots, L_{2(K-1)n_2}^{(f)} \\ L_{2K1}^{(f)}, \dots, L_{2Kn_2}^{(f)} \end{array} \right], \end{aligned} \quad (9)$$

$$\nabla_2^{(f)} = \begin{bmatrix} (L_{221}^{(f)} - L_{211}^{(f)}) & \dots & (L_{22n_2}^{(f)} - L_{21n_2}^{(f)}) \\ (L_{231}^{(f)} - L_{221}^{(f)}) & \dots & (L_{23n_2}^{(f)} - L_{22n_2}^{(f)}) \\ \vdots & & \vdots \\ (L_{2(K-1)1}^{(f)} - L_{2(K-2)1}^{(f)}) & \dots, & (L_{2(K-1)n_2}^{(f)} - L_{2(K-2)n_2}^{(f)}) \\ (L_{2K1}^{(f)} - L_{2(K-1)1}^{(f)}) & \dots, & (L_{2Kn_2}^{(f)} - L_{2(K-1)n_2}^{(f)}) \end{bmatrix}, \quad (10)$$

$$\bar{\nabla}_2^{(f)} = \frac{1}{n_2} \nabla_2^{(f)} \mathbf{1}_{n_2 \times 1} \quad (11)$$

and, denoting the columns of $\nabla_2^{(f)}$ as $\{\nabla_{2u}^{(f)}\}_{u=1}^{n_2}$,

$$\left\{ x_{2u}^{(f)} = \frac{180}{\pi} \arccos \left(\frac{(\nabla_{2u}^{(f)})^\top \bar{\nabla}_2^{(f)}}{\|\nabla_{2u}^{(f)}\| \|\bar{\nabla}_2^{(f)}\|} \right) \right\}_{u=1}^{n_2}. \quad (12)$$

And equivalently for $\mathbf{W}_1 = (\mathbf{y}_{11}, \dots, \mathbf{y}_{1n_1})$ —the rearranged version of a $(n \times n)$ window of test data at location ij in \mathbf{X} and the columns of $\nabla_2^{(f)}$ in equation 10— $\{\nabla_{2u}^{(f)}\}_{u=1}^{n_2}$, we have

$$\left\{ x_{1u}^{(f)} = \frac{180}{\pi} \arccos \left(\frac{(\nabla_{2u}^{(f)})^\top \bar{\nabla}_1}{\|\nabla_{2u}^{(f)}\| \|\bar{\nabla}_1\|} \right) \right\}_{u=1}^{n_2}. \quad (13)$$

From equation 12 and 13, the following two univariate sequences will be used as inputs to the AVT detector:

$$x_2^{(f)} = (x_{21}^{(f)}, x_{22}^{(f)}, \dots, x_{2n_2}^{(f)}) \quad (14)$$

and

$$x_1^{(f)} = (x_{11}^{(f)}, x_{12}^{(f)}, \dots, x_{1n_2}^{(f)}), \quad (15)$$

where $1 \leq f \leq N$.

Following the discussion that led to equation 5, the AVT detector is implemented as follows:

$$\tilde{Z}_{AVT}^{(ij)} = \min_{1 \leq f \leq N} Z_{AVT}^{(ij)(f)}, \quad (16)$$

where,

$$Z_{AVT}^{(ij)(f)} = n_2 \frac{(S_2^{2(f)} - S_{union}^{2(f)})^2}{\hat{\zeta}_2^{2(f)}}, \quad (17)$$

S_2^2 is the sample variance of $x_2^{(f)}$ in (3.10), $S_{\text{union}}^{2(f)}$ is the sample variance of $(x_2^{(f)}, x_1^{(f)})$ —the combined sample using equation 14 and 15, and—for $\bar{x}_2^{(f)}$ denoting the sample mean of $x_2^{(f)}$ —

$$\hat{\zeta}_2^{2(f)} = \sum_{u=1}^{n_2} \frac{[(x_{2u}^{(f)} - \bar{x}_2^{(f)})^2 - S_2^{2(f)}]^2}{n_2 - 1}. \quad (18)$$

After computing all $\{\tilde{Z}_{\text{AVT}}^{(ij)}\}_{i=1, j=1}^{R-n-1, C-n-1}$ using equation 16 and indexing them with the given repetition g ($1 \leq g \leq M$), a 2-dim output surface $\tilde{\mathbf{Z}}_{\text{AVT}}^{(g)}$ is produced,

$$\tilde{\mathbf{Z}}_{\text{AVT}}^{(g)} = \begin{bmatrix} \tilde{Z}_{\text{AVT}}^{(11)(g)}, & \dots, & \tilde{Z}_{\text{AVT}}^{[1(C-n-1)](g)} \\ \vdots & \vdots & \vdots \\ \tilde{Z}_{\text{AVT}}^{[(R-n-1)1](g)}, & \dots, & \tilde{Z}_{\text{AVT}}^{[(R-n-1)(C-n-1)](g)} \end{bmatrix}, \quad (19)$$

which leads to AVT's final output surface \mathbf{Z}_{AVT} ,

$$\mathbf{Z}_{\text{AVT}} = \begin{bmatrix} \sum_{g=1}^M \tilde{Z}_{\text{AVT}}^{(11)(g)}, & \dots, & \sum_{g=1}^M \tilde{Z}_{\text{AVT}}^{[1(C-n-1)](g)} \\ \vdots & \vdots & \vdots \\ \sum_{g=1}^M \tilde{Z}_{\text{AVT}}^{[(R-n-1)1](g)}, & \dots, & \sum_{g=1}^M \tilde{Z}_{\text{AVT}}^{[(R-n-1)(C-n-1)](g)} \end{bmatrix}. \quad (20)$$

For the remainder of this report, we will refer to parallel random sampling as PRS and, consequently, to equations 8 and 20 as PRS-RX and PRS-AVT, respectively.

4. Summary of Results

This section focuses on the application of the PRS approach, as discussed in section 3, to the autonomous GV anomaly detection problem. No prior information (e.g., spectral library, expected target scales, any knowledge about the scenario) is used, except for the comparative analysis discussed later in this section. Since this approach requires an effective anomaly detector as its base detector, and results in reference 18 show that the two-step univariate detection techniques are more effective for testing difficult simulated cases than existing multivariate detection techniques, most of the results presented herein were obtained using PRS-AVT. Initial results using PRS-AVT and PRS-RX are shown in subsection 4.1. Applying PRS-AVT to data collected recently (May/June 2008) at Picatinny Arsenal, NJ, additional results are shown in subsection 4.2. The recent data exemplify various scene conditions (e.g., fog, partially overcast). Subsection 4.1 focuses on first checking whether PRS (using an effective detector)

works; subsection 4.2 focuses on the performance robustness of PRS-AVT to changing illumination environment and atmospheric conditions.

4.1 Initial Results

PRS-AVT was initially applied to Cube 1, Cube 2, Cube 3, and Cube 4 (see figure 1) to test for scene (spectral) anomalies, obtaining excellent results—they are shown in this subsection. PRS-RX was also applied to Cube 3 for comparison purposes.

We begin by first showing how parameters N and M affect the output of PRS-AVT testing Cube 1 (figure 6). Figure 6 (top right and bottom left) represent two different outcomes for \mathbf{Z}_{AVT} in equation 20, where $n \times n$ was fixed at once to 20×20 (for all data blocks and window sizes) and parameters q , N , and M were set to ($q = 0.1$; $N = 3$; $M = 3$)—top right display—and ($q = 0.1$; $N = 22$; $M = 40$)—bottom left display. (These output surfaces, which for displaying purposes were extended to the size of Cube 1, are displayed using a pseudo-color map, such that, the brighter the pixel values in those surfaces, the stronger it is the evidence of anomalies at those pixel locations, relative to randomly selected blocks of data. Also, for calibration purposes, the single motor vehicle at the scene’s center right has about 25,000 pixels, which means that a 20×20 window would test 63 non-overlapping pixel locations over that target; but this target would yield significantly more than 63 pixels in the output surface since sliding windows overlap.) The top right output surface displays an example when N is not set sufficiently high in order to adequately represent the clutter background. In this case, three blocks of data were randomly selected from the scene (most likely from the open field area, since it is the largest area in the scene), and used by the AVT detector to suppress (according to $\tilde{\mathbf{Z}}_{AVT}^{(g)}$ ($g = 1, \dots, M$) in equation 19) the open field in Cube 1, not only once, but most likely $M = 3$ times. As a result, the three motor vehicles and the canopy area on the upper portion of that scene were accentuated relative to the open field. Initially, we ignored the Binomial distribution model and set parameters N and M intentionally low in order to test Cube 1 and show the undesired result in figure 6 (top right).

If M were set much higher (e.g., 30), with other parameters fixed, one or more $\tilde{\mathbf{Z}}_{AVT}^{(g)}$ would most likely have the tree area also suppressed, but since all of $\tilde{\mathbf{Z}}_{AVT}^{(g)}$ are pixelwise summed (see equation 20) that tree area (although smaller than the open field, yet significantly larger than individual candidate targets) would still be accentuated relative to the open field. The results shown in figure 6 (top right) gave us the initial confidence that PRS seems to work as intended. We then used the Binomial distribution model to guide us on setting N and M , which is conditional on a sensible q .

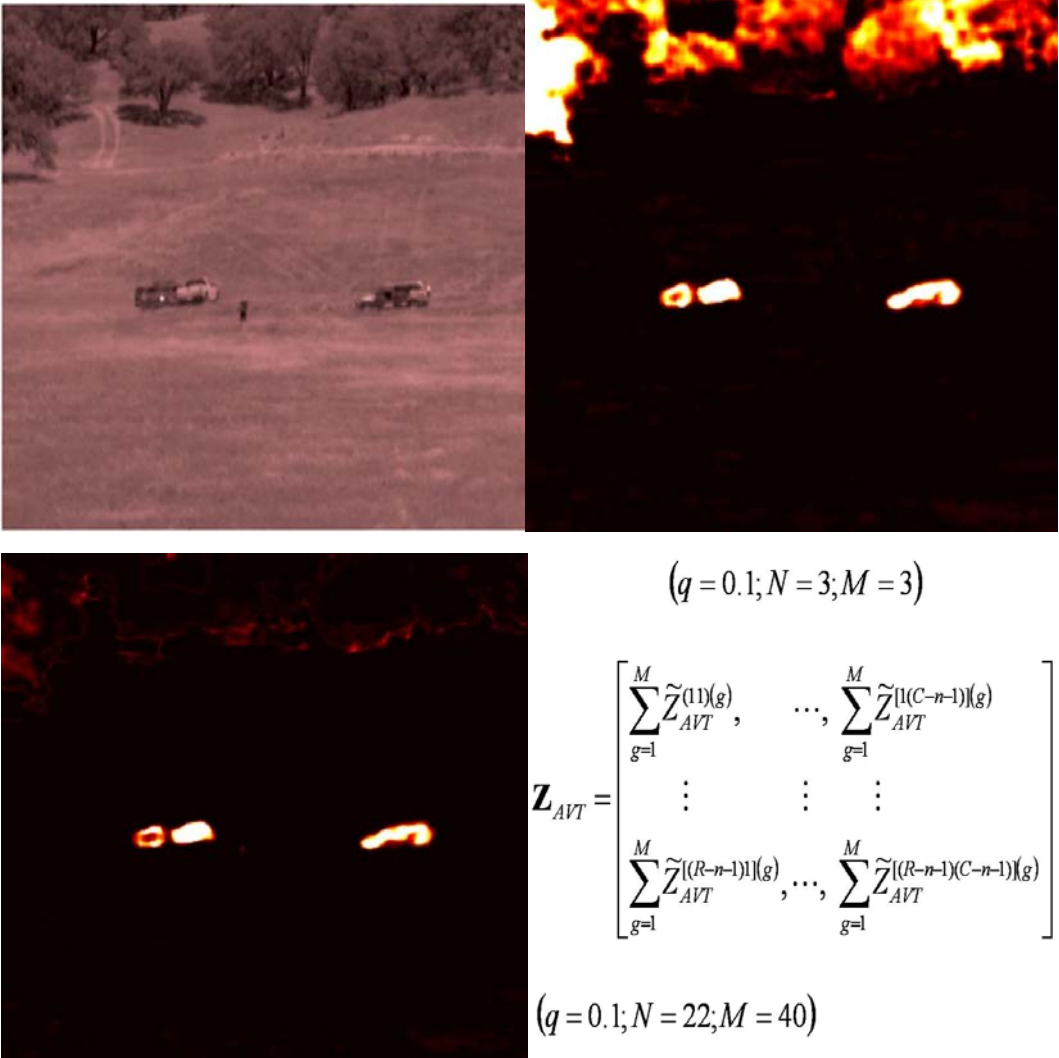


Figure 6. PRS-AVT results on Cube 1 (top left) for scene anomalies; output surface (top right) using parameters $(q = 0.1; N = 3; M = 3)$; and output surface (bottom left) using parameters $(q = 0.1; N = 22; M = 40)$. Brighter pixels values in the output surfaces correspond to higher confidence on the presence of anomalies in the imagery, relative to randomly selected blocks of data. Also, notice that since \mathbf{Z}_{AVT} is a sum of results, bright clusters in those surfaces are smooth clusters.

For most remote sensing applications, targets (if present in the scene) will cover no more than 10% of the imagery spatial area. For instance, the motor vehicle having 25,000 pixels in Cube 1 covers 6.1% of the imagery area $\left(\frac{25000}{409600}\right)$. So, we fix at once $q = 0.1$ as a robust choice. The binomial distribution plot in figure 3, for $q = 0.1$, shows that $N = 22$ yields an upper bound contamination probability $P_g(m \geq 1) \approx 0.9$ ($1 \leq g \leq M$), and the plot in figure 4 shows a corresponding cumulative contamination probability $\tilde{P}(\tilde{m} = M) \approx 0.0$ for $M = 40$. The output surface shown in figure 6 (bottom left) is the result using PRS-AVT to test Cube 1 having parameters set to $(q = 0.1; N = 22; M = 41)$. That output surface shows the manmade objects

(three motor vehicles) clearly accentuated relative to the unknown cluttered environment, given that no prior information is used about the materials composing the clutter background, or about whether targets are present in the scene, or about targets' scales relative to other object structures in the imagery. But notice in figure 6 that the standing person in the scene center is not detected, possibly because the window size might be too large and/or there must have some materials in that background (randomly selected) spectrally similar to the materials representing that person (e.g., pants, shirt, skin). Figures 7 and 8 show additional results.

Figure 7 shows results using PRS-AVT to test Cube 2 and Cube 3, and figure 8 shows results using PRS-AVT to test Cube 4, which represents a particularly difficult case of clutter suppression. Parameters were set to ($q = 0.1$; $N = 22$; $M = 40$) for the three cubes.



Figure 7. PRS-AVT results on Cube 2 (top left) and Cube 3 (bottom left), where corresponding output surfaces are shown immediately to the right of the cube displays. Parameters were set to ($q = 0.1$; $N = 22$; $M = 40$).

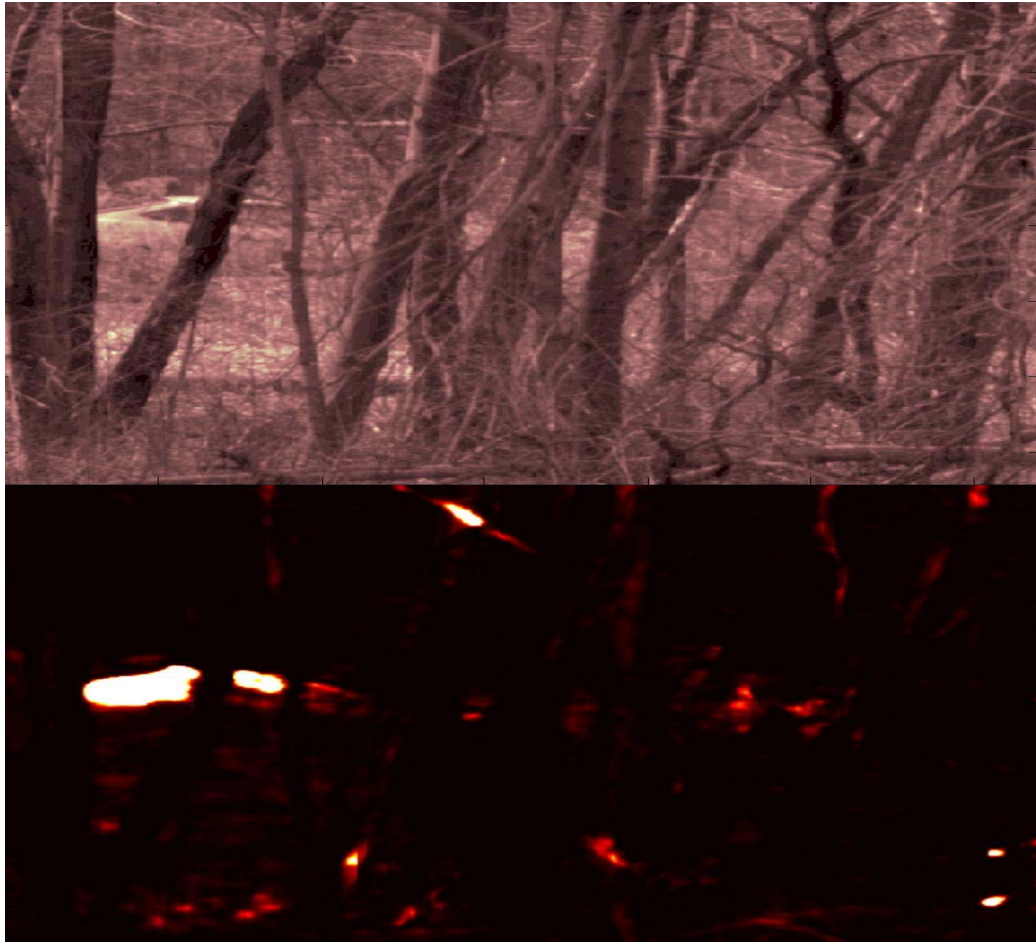


Figure 8. PRS-AVT results on Cube 4 (left), and corresponding output surface (right). Parameters were set to ($q = 0.1$; $N = 22$; $M = 40$). Cube 4 exemplifies a hard case for autonomous clutter suppression.

The output results shown in figures 6, 7, and 8, using parameters set to ($q = \mathbf{0.1}$; $N = \mathbf{22}$; $M = \mathbf{40}$), are excellent results for the given application, especially for Cube 3 and Cube 4, both clearly showing the presence of a motor vehicle highly accentuated—one in tree shades and another parked behind a heavily cluttered environment. These results ensure to us that the idea behind the PRS approach works, as intended, but the overall results might dependent on the effectiveness of its core anomaly detection technique. Figure 9 shows a qualitative comparison between using PRS-AVT and PRS-RX to test Cube 3.

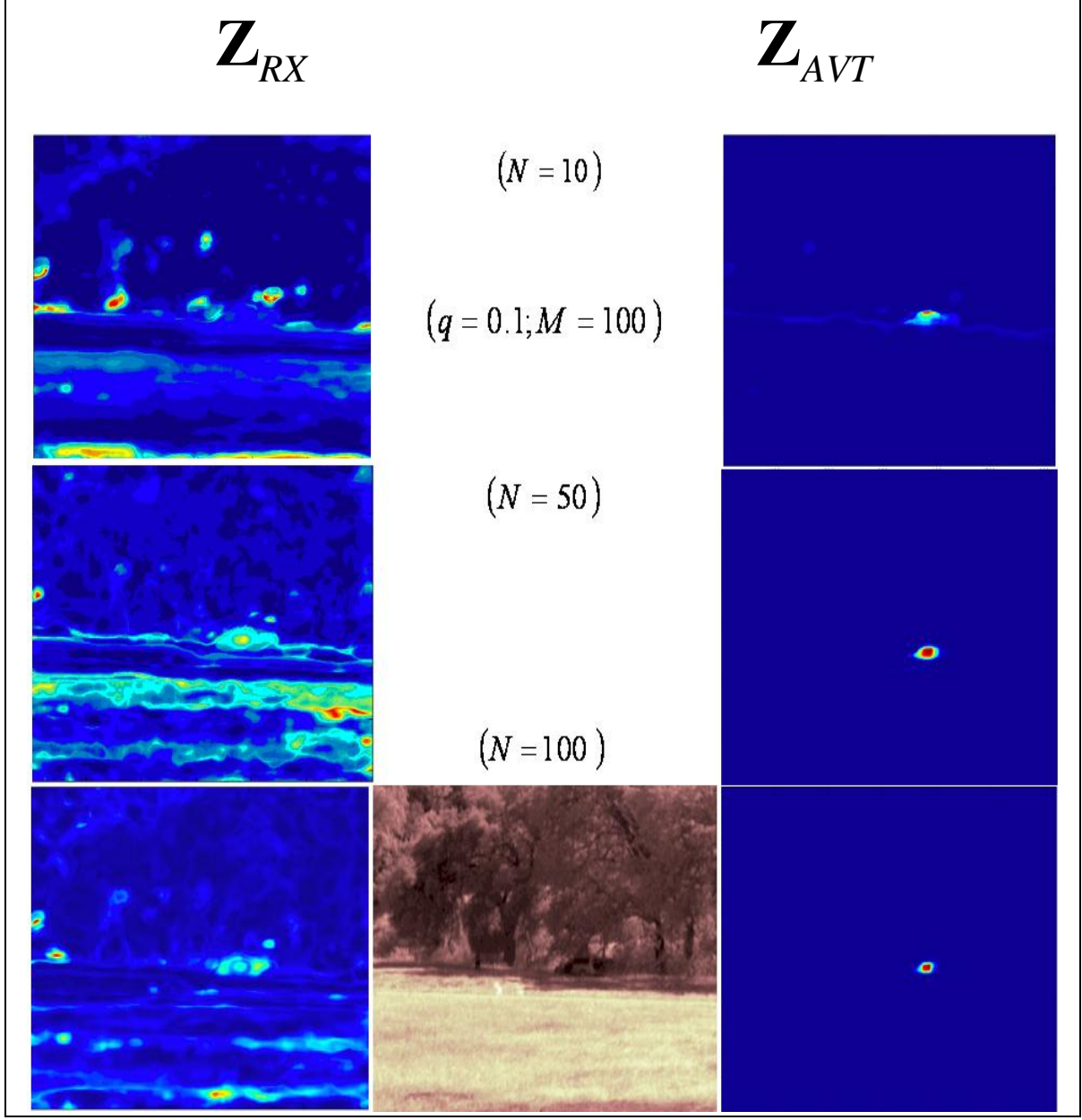


Figure 9. Comparison results for PRS-AVT and PRS-RX on Cube 3 (bottom center) by setting N to three different values (10, 50, and 100); the corresponding PRS-RX output surfaces are shown in the left column, and the corresponding PRS-AVT output surfaces are shown in the right column.

For the results presented in figure 9, the window size $(n \times n) = (20 \times 20)$ and parameters $(q = 0.1; M = 100)$ were fixed, but N varied ($N = 10, 50, 100$). Using $M = 100$ (a high number of repetitions—it took two weeks to obtain results shown in figure 9 using the MATLAB software environment and a Pentium IV personal computer), we have confidence that the overall cumulative probabilities of contamination for both PRS-AVT and PRS-RX are equally low for the chosen values of N . In doing so, we can now check the sensitivity of the AVT and RX detectors to different values of N . Under these settings, the detector that can show the lesser

sensitivity to varying N is more desired. Sensitivity can be qualitatively checked by inspection of figure 9, i.e., the observed changes on the output surface of a given detector as N changes. PRS-RX results are shown in the left column (figure 9), and PRS-AVT output surfaces are shown in the right column (figure 9), where, from the top, N values were changed from 10, 50, to 100. Both sets of output surfaces use the same standard pseudo-color map (*rainbow*, which is available in MATLAB) for displaying purposes. By inspection, the output surfaces in figure 9 clearly show a higher sensitivity of the RX detector to a varying N compared to the AVT detector. These output surfaces were extended to match the approximate size of the imagery spatial area of Cube 3 in figure 9. According to available ground truth information about the data collection, the visible clusters approximately at the center of all three PRS-AVT output surfaces correspond to the pixel locations where a motor vehicle happens to be present under tree shades. Similar clusters are also shown at about the same pixel locations in PRS-RX output surfaces using $N = 50$ and $N = 100$, but with the cost of having clusters of similar or greater strength elsewhere in the imagery (false positives) covering some 15% to 20% of the imagery spatial area. Using $N = 10$, the corresponding PRS-RX output surface shows that the anomaly strength at the target pixel locations are similar or greater than the strength of no more than 50% or so of all pixel locations in the imagery, which means that if a threshold is set to detect target pixels, about 50% of the imagery would show up as being anomalous to the clutter background.

We will now address the robustness of the PRS-AVT testing HS data collected under various environmental conditions.

4.2 Adaptive Threshold Under Various Environment Conditions

The goal in this subsection is to establish an adaptive threshold method and then to test PRS-AVT for robustness using real HS imagery collected under various environmental conditions. But before we address the adaptive threshold requirement, we will first briefly introduce the additional dataset used to produce results for this subsection, followed by a brief discussion on automatically setting parameters N and M , given q .

4.2.1 Description of Additional Data

Figure 10 depicts photos taken at a target site under various environmental conditions at the U.S. Army Armament Research, Development, and Engineering Center (ARDEC), Picatinny Arsenal, NJ. The target site in figure 10 features heavy clusters of trees, surrounding an open grassy field, and a dirt road leading to targets. There are two targets at that site; both are validated surrogates of military tanks, which imply that their physical appearances are similar to the actual tanks, and they were painted using genuine paints of the targets they represent. Using the SOC-700 HS imaging system, HS VNIR data were recently collected (May/June 2008) from a tower standing about 0.7 km from the target site, capturing reflectance of the same site under seven different conditions:

1. Clear sunny day (noon) at a higher elevation (data collected at a higher elevation angle relative to the remainder viewing perspectives in this set, except in condition 7)
2. Clear sunny day (afternoon) at a lower elevation
3. Clear sunny late afternoon (sun light is weaker, objects cast long shadows)
4. Cloudy day (sun light energy is attenuated by some amount)
5. Fog above the targets (upper fog)
6. Targets immersed in fog (lower fog)
7. Partially overcast (where the targets are present on the overcastted portion of the scene and elevation angle is the same as in condition 1).

These various conditions are known to challenge target detection/classification algorithms because they can significantly change the spectral characteristics of a particular material (e.g., paint), see, for instance, reference 36.

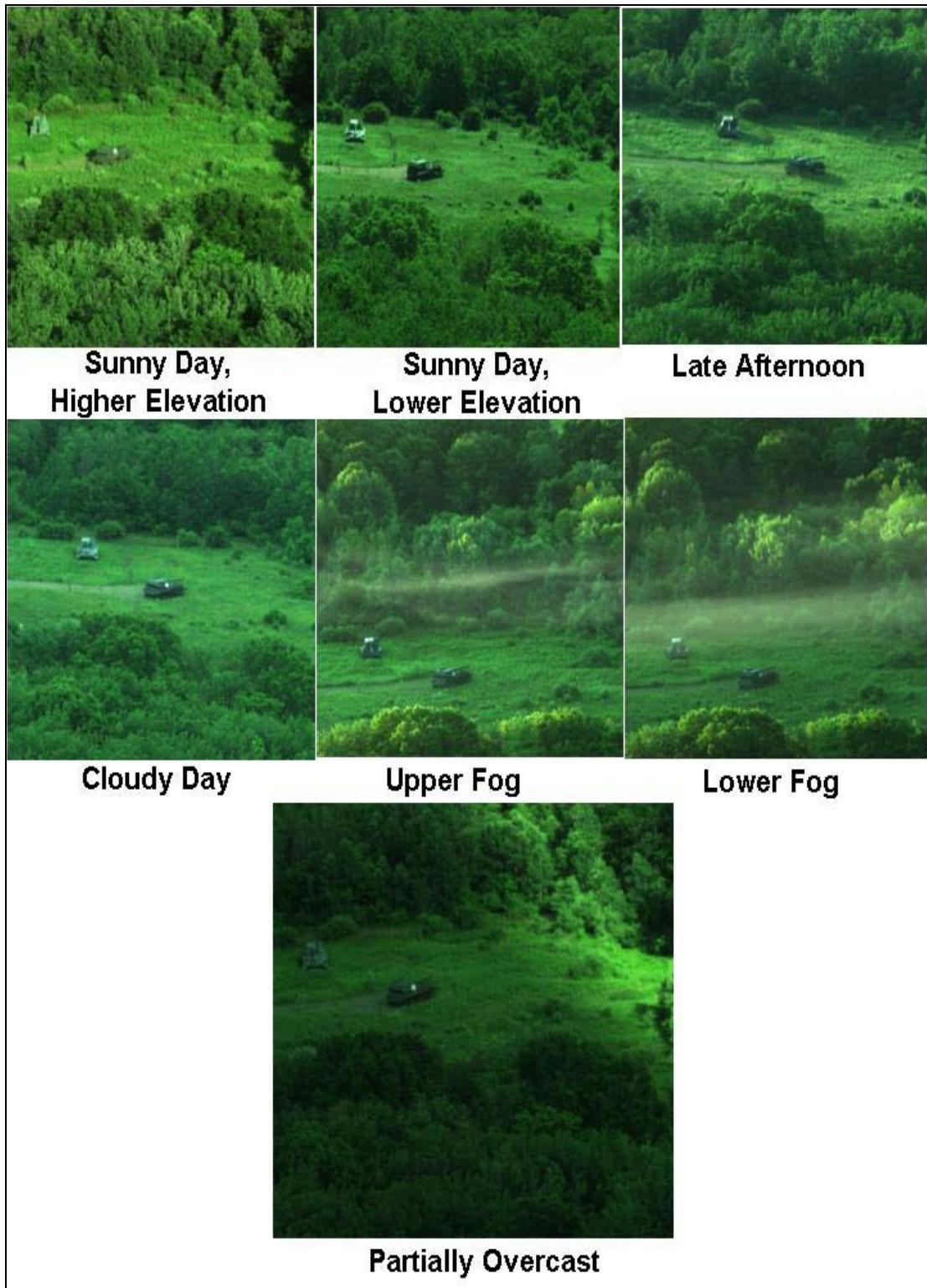


Figure 10. A target site under different environmental conditions.

4.2.2 Automatic Parameter Setting

For remote sensing applications, it is often desired to enable a machine to automatically set algorithm parameters. On this note, we can automate the setting process of parameters N and M , given q .

To properly function, the PRS approach requires an adequately large N , which undesirably increases the contamination probability $P(m \geq 1)$ per repetition, and an adequately large M , which desirably decreases the overall cumulative contamination probability $\tilde{P}(\tilde{m} = M)$ of the PRS approach for M repetitions. From equations 1, 2, and 4, using the log of base 10, direct transformation leads to

$$N = \frac{\log[1 - P(m \geq 1)]}{\log(1 - q)} \quad (21)$$

and

$$M = \frac{\log[\tilde{P}(\tilde{m} = M)]}{\log[1 - (1 - q)^N]}. \quad (22)$$

For any given q , we can fix the values of $P(m \geq 1)$ and $\tilde{P}(\tilde{m} = M)$, and obtain N and M directly using equations 21 and 22, respectively. As guideline, $P(m \geq 1)$ should be set high, but less than 1.0, so that N can also be relatively high and $\tilde{P}(\tilde{m} = M) < 1.0$; $\tilde{P}(\tilde{m} = M)$ should be set very low, near zero. The good news is that the actual values of $P(m \geq 1)$ and $\tilde{P}(\tilde{m} = M)$ are unimportant, as long as the guideline is followed. As an example, we could fix $P(m \geq 1) = 0.90$ and $\tilde{P}(\tilde{m} = M) = 0.01$, and for $q = 0.05$, we obtain directly from equations 21 and 22 parameter values $N \approx 45$ and $M \approx 44$. (Since N and M are defined as integers, these numbers are rounded off \approx .) For consistency with initial results discussed in subsection 4.1, we will fix at once $q = 0.10$, $P(m \geq 1) = 0.90$, and $P_R(m_R = M) = 0.015$, which using equations 21 and 22 yield $N \approx 22$ and $M \approx 40$.

4.2.3 Adaptive Cutoff Threshold

An adaptive cutoff threshold is also desired for remote sensing applications due to the various environmental conditions a scene can be exposed to, and to the diverse clutter background in different geographic locations across the world. For the PRS approach, we propose to take the fused output surface, in the case of AVT, \mathbf{Z}_{AVT} in equation 20, and estimate both the mean and standard deviation (STD or sigma) using this surface's pixel values as input. Denoting $\mu_{\mathbf{Z}_{AVT}}$ and $\sigma_{\mathbf{Z}_{AVT}}$ the sample average and the sample STD, respectively, an adaptive cutoff threshold (a scalar) is obtained as

$$T(a) = \mu_{\mathbf{Z}_{AVT}} + a\sigma_{\mathbf{Z}_{AVT}}, \quad (23)$$

where $a > 0.0$ is a constant and, using equations 19 and 20,

$$\mu_{\mathbf{Z}_{AVT}} = \frac{1}{(R-n-1)(C-n-1)} \sum_{i=1}^{(R-n-1)} \sum_{j=1}^{(C-n-1)} \left[\sum_{g=1}^M \tilde{Z}_{AVT}^{(ij)(g)} \right], \quad (24)$$

and

$$\sigma_{\mathbf{Z}_{AVT}} = \sqrt{\frac{\sum_{i=1}^{(R-n-1)} \sum_{j=1}^{(C-n-1)} \left[\left(\sum_{g=1}^M \tilde{Z}_{AVT}^{(ij)(g)} \right) - \mu_{\mathbf{Z}_{AVT}} \right]^2}{(R-n-1)(C-n-1)-1}}. \quad (25)$$

If equations 24 and 25 happens to be too sensitive to a relatively small number of pixels values in \mathbf{Z}_{AVT} , then one could use the average median, in place of the sample mean, and a less sensitive estimate for STD. After experimenting with the latter route, we did not see a need to follow it; hence, we chose to use equations 23, 24, and 25 to test the additional data cubes shown in figure 10.

The SOC-700 imaging system can record the HS VNIR data cube of a site while taking a photo of the same viewing sight of the HS imager. Figure 10 depicts only the photos of the target site. The HS data cubes used for this experiment have dimensions $R = 640$ by $C = 640$ pixels by $K = 120$ spectral bands between 0.38 and 0.97 μm .

In order to test the additional data depicted in figure 10, we set the data block size and testing window size to be the same, or $(n \times n) = (20 \times 20)$; $q = 0.10$; $P(m \geq 1) = 0.90$, which using equation 21 yields $N = 22$; $P_R(m_R = M) = 0.015$, which using equation 22 yields $M = 40$; and the adaptive cutoff threshold $T(a) = \mu_{\mathbf{Z}_{AVT}} + a\sigma_{\mathbf{Z}_{AVT}}$, see equation 23, set initially to $T(10)$ and $T(30)$.

We tested these additional data cubes but exhibited the corresponding results differently from the way results were exhibited in subsection 4.1. Figure 11 depicts some of those results using PRS-AVT to test the HS data cube named *Cloudy Day*. In figure 11, the photo representing this cube is shown at the top left; the top right shows the thresholded fused-output surface using $T(10)$; the bottom right shows the thresholded fused surface overlaid on the photo (the fused output surface and its thresholded version were automatically extended to the known photo size, as part of the overlaying process); and the bottom left shows the thresholded fused-output surface using $T(30)$.

Notice in figure 11 that at 10 sigma both targets are fully detected, and the dirt road shows up as false positives. At 30 sigma, an autonomous and untrained machine—having no prior information about the target scales/shapes or materials composing the clutter background—can detect both targets with no false alarms, figure 11 (bottom left). Figure 12 shows additional results.

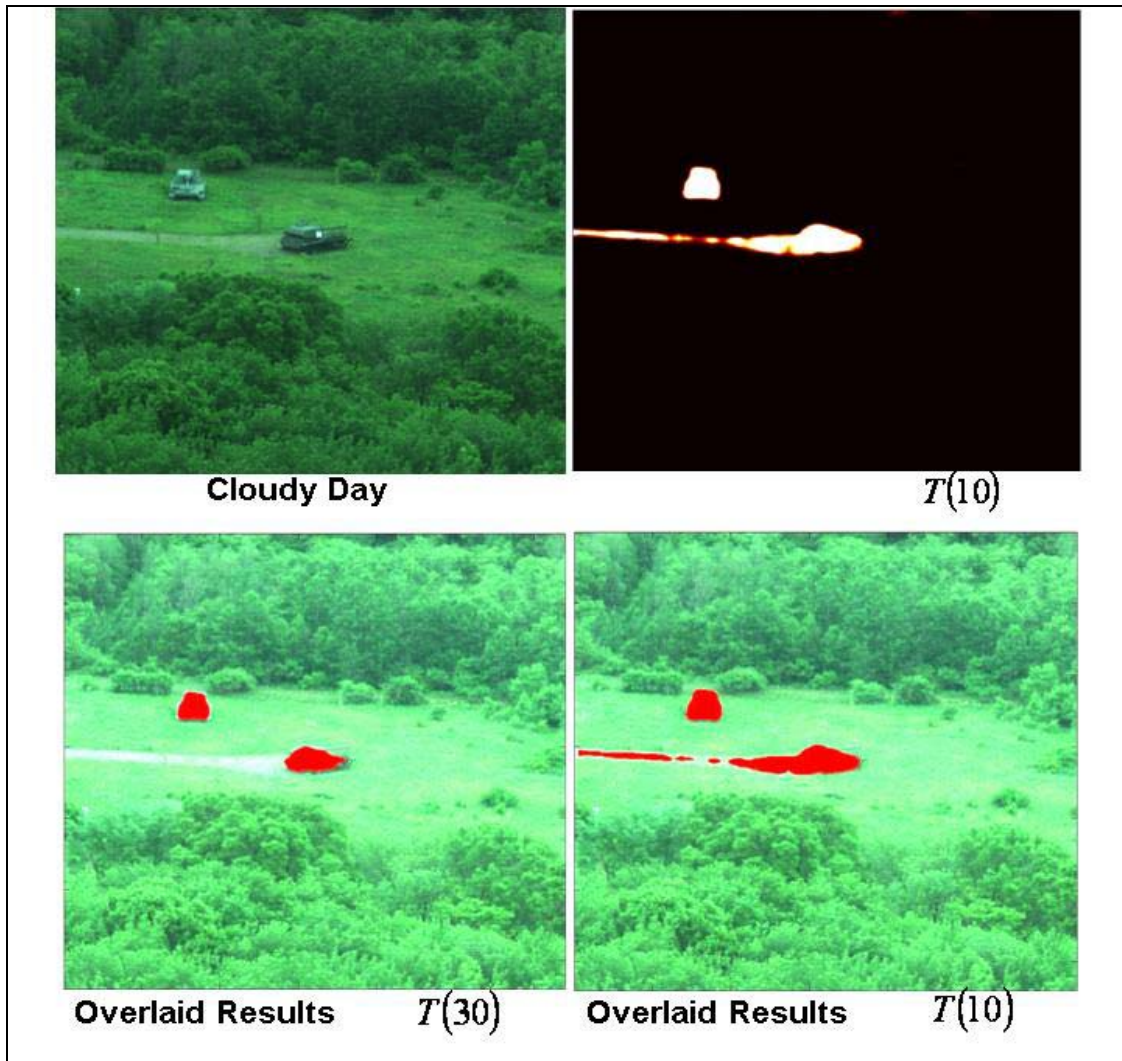


Figure 11. PRS-AVT thresholded fused-output surface (top right) using parameters ($q = 0.1$; $N = 22$; $M = 40$) and $T(10)$; Overlaid results using threshold $T(10)$ (bottom right) and $T(30)$ (bottom left). At 30 sigma, both targets are fully detected with no false positives. Because of the targets' different angular orientations, they appear to have different scales and shapes.

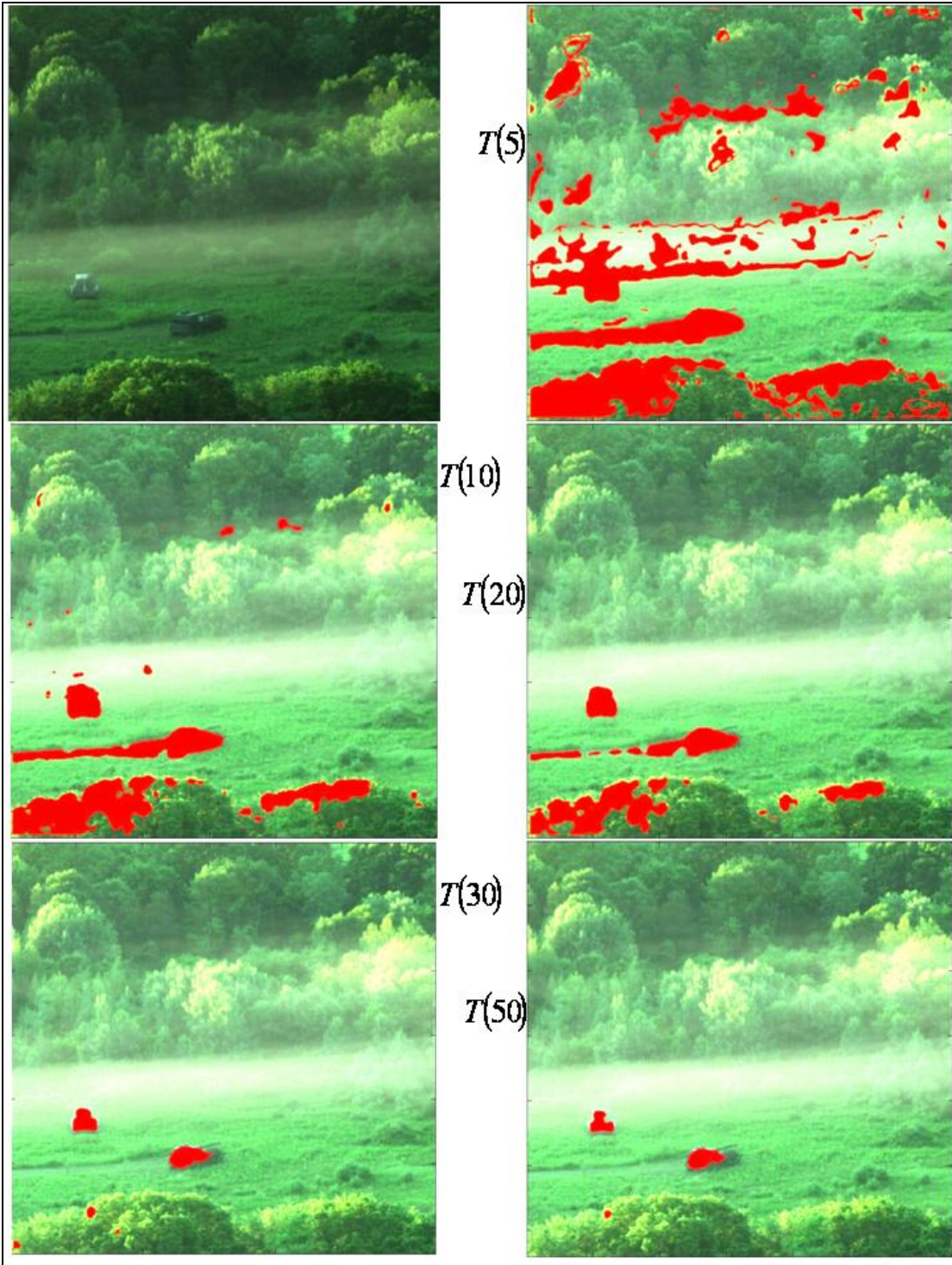


Figure 12. PRS-AVT overlaid results for Lower Fog, using parameters ($q = 0.1$; $N = 22$; $M = 40$) and adaptive thresholds $T(5)$, $T(10)$, $T(20)$, $T(30)$, and $T(50)$.

Figure 12 depicts the PRS-AVT results using the HS data cube named *Lower Fog* (arguably the most difficult one in this additional dataset for autonomous anomaly detection tasks), and applying the following thresholds: $T(5)$, $T(10)$, $T(20)$, $T(30)$, and $T(50)$, where the first column

in figure 12 shows results for $T(10)$ and $T(30)$, and the second column shows $T(5)$, $T(20)$, and $T(50)$. Notice that at 10 sigma, the fog over the valley causes PRS-AVT to quadruple the false alarm proportion relative to results shown in figure 11 (bottom right) for the same scene on a cloudy day. But at 30 sigma, both targets are comparably detected between HS data cubes *Lower Fog* and *Cloudy Day*, producing negligible false positives (notice in figure 12, first column bottom surface, one can see very small clusters of false positives at the lower left of that surface). At 50 sigma, the detection and false alarm proportions are comparable between results using $T(30)$ and $T(50)$, which strongly suggests that PRS-AVT is capable of accentuating scene anomalies under adverse conditions. In order to check this, we tested the remainder data cubes using PRS-AVT (figure 13).

In figure 13, tested cubes are shown in rows 1 and 4 (from the top), and—applying an adaptive threshold at $T(30)$ —the corresponding overlaid results are shown in rows 2 and 3. Both targets are detected with virtually no false positives, except for the negligible false positive very small clusters shown on results for *Lower Fog* (lower left in overlaid surface). Those results suggest that the PRS approach, having an effective anomaly detection technique as its base detector, seems to be a robust approach for different data collection conditions.

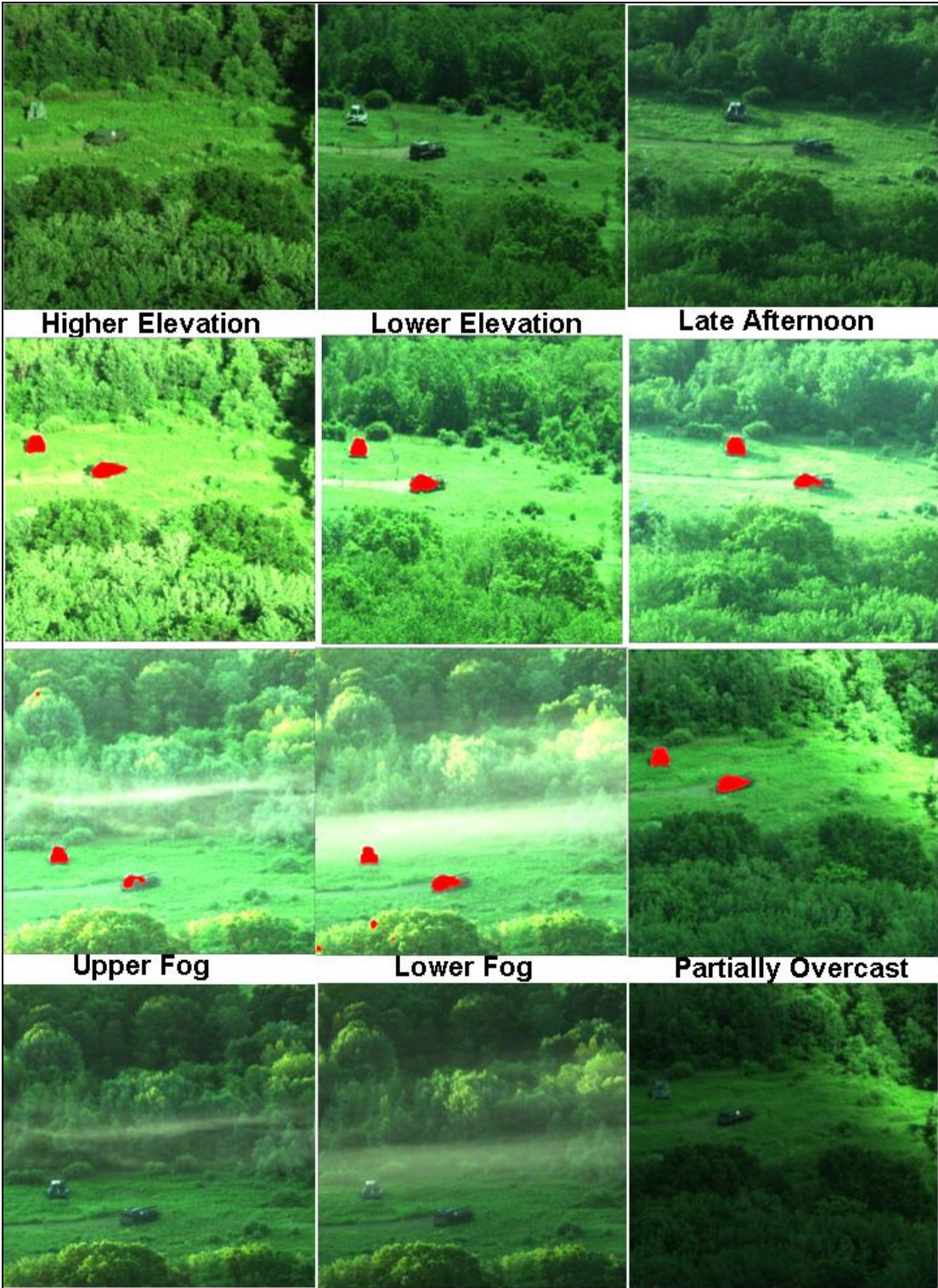


Figure 13. PRS-AVT overlaid results, using parameters ($q = 0.1$; $N = 22$; $M = 40$) and adaptive threshold $T(30)$. In all cases, PRS-AVT yielded virtually zero false alarms detecting both targets.

5. Conclusion

This report has proposed and examined the performance of an autonomous approach for the GV anomaly detection problem using real HS data cubes. The approach is generalized in the sense that it can be used with any detection technique, although this report also showed that the effectiveness of the chosen base detector will significantly affect the test results. The approach applies random sampling of the imagery and repeats the sampling process in order to mitigate the probability of contamination (spectral samples of candidate targets being used as clutter background reference samples). As such, the approach requires no prior information (e.g., a spectral library of the clutter background and/or target, target size, or shape), and, therefore, is free from training requirements. This report showed that the PRS approach can be modeled by the binomial family of distributions, where the only target related parameter q (the upper bound proportion of target pixels potentially covering the spatial area of the imagery) is robust—thus invariant—to different sizes and shapes of targets, number of targets present in the scene, target aspect angle, partially obscured targets, or sensor viewing perspective. Binomial distribution plots were used to set other parameters: N (number of randomly selected blocks of data) and M (number of process repetitions). This report also showed how N and M can be automatically set using a simple guideline, and how to implement an adaptive cutoff threshold method with PRS.

The PRS-AVT approach, in particular, was applied to real HS data cubes yielding excellent results for different target deployments (target in an open field, target in tree shades, and target behind heavy wooded region), different environmental and illumination conditions (conditions as diverse as having fog over or immersing the targets, partially overcast, and different elevation angles and times of the day), and different clutter backgrounds (California valley, New Jersey wooded areas). Finally, a comparative analysis was presented to show the effectiveness of using the univariate anomaly detection technique (AVT) over a more conventional multivariate anomaly detection technique (RX) to the GV anomaly detection problem.

References

1. Campbell, J. B. *Introduction to Remote Sensing*; 2nd ed. New York: Guilford, 1996.
2. Lillesand, T. M.; Kiefer, R. W. *Remote Sensing and Image Interpretation*; New York: Wiley, 1994.
3. Schowengerdt, R. A. *Remote Sensing, Models and Methods for Image Processing*; 2nd ed. San Diego, CA: Academic Press, 1997.
4. Manolakis, D.; Marden, D.; Shaw, G. Target detection algorithms for hyperspectral imaging applications. *Lincoln Laboratory Journal* **2003**, *14* (1).
5. Schott, J. R. *Remote Sensing, The Image Chain Approach*; Oxford University Press, New York, NY, 1997.
6. Fukunaga, K. *Introduction to Statistical Pattern Recognition*; 2nd edition, Academic Press, Inc., San Diego, CA, 1990.
7. Crist, E.; Schwartz, C.; Stocker, A. Pairwise adaptive linear matched-filter algorithm. In *Proc DARPA Adaptive Spectral Reconnaissance Algorithm Workshop*, January 1999.
8. Kwon, Heesung; Nasrabadi, Nasser M. Kernel Spectral Matched Filter for Hyperspectral Imagery. *J. of Computer Vision* **2007**, *71* (2), 123–253.
9. Grossmann, J.; Bowles, J.; Hass, D.; Antoniades, J.; Grunes, M.; Palmadesso, P.; Gillis, D.; Tsang, K.; Baumback, M.; Daniel, M.; Fisher, J.; Triandaf, I. Hyperspectral analysis and target detection system for the adaptive-spectral reconnaissance program (ASRP). *Proc SPIE April 1998*, *3372*, 2–13.
10. Chang, C.; Zhao, X.; Althouse, M.; Pan, J. Least squares subspace projection approach to mixed pixel classification for hyperspectral images. *IEEE Trans. Geosci. Remote Sensing* **May 1998**, *36*, 898–912.
11. Slater, D.; Healey, G. Exploiting an atmospheric model for automated invariant material identification in hyperspectral imagery. *Proc. SPIE April 1998*, *3372*, 60–71.
12. Stocker, A. Stochastic expectation maximization (SEM) algorithm. In *Proc. DARPA Adaptive Spectral Reconnaissance Algorithm Workshop*, January 1999.
13. Masson, P.; Pieczynski, W. SEM algorithm and unsupervised statistical segmentation of satellite images. *IEEE Trans. Geosci. Remote Sensing* **May 1993**, *31*, 618–633.

14. Yu, X.; Hoff, L.; Reed, I.; Chen, A.; Stotts, L. Automatic target detection and recognition in multiband imagery: A unified ML detection and estimation approach. *IEEE Tran. Image Processing* **January 1997**, *6*, 143–156.
15. Kwon, H.; Nasrabadi, N. Kernel RX-algorithm: a nonlinear anomaly detector for hyperspectral. *IEEE Trans. on Geoscience and Remote Sensing* **February 2005**, *43* (2).
16. Kwon, H.; Der, S. Z.; Nasrabadi, N. M. Adaptive anomaly detection using subspace separation for hyperspectral imgery. *Opt. Eng.* **November 2003**, *42* (11), 3342–3351.
17. Schokopf, B.; Smola, A. J.; Muller, K-R. Kernel principal component analysis. *Neural Computation* **1999**, *10*, 1299–1319.
18. Rosario, D. *Alternative Asymmetric Hypothesis Tests for Hyperspectral Imagery*; ARL-TR-3712; U.S. Army Research Laboratory: Adelphi, MD, February 2006.
19. Vane, G.; Green, R. O.; Chrien, T. Go.; Enmark, H. T.; Hansen, E. G.; Porter, W. M. The airborne visible/infrared imaging spectrometer (AVIRIS). *Remote Sensing of the Environment* **1993**, *44*, 127–143.
20. Surface Optics Corporation, Website: <http://www.surfaceoptics.com> (September 2008).
21. Schott, J. R. *Remote Sensing: The Imaging Chaing Approach*; Oxford University Press, New York, 1997.
22. Duda, R. O.; Hart, P. E. *Pattern Classification Scene Anal.*; Second Edition, New York: J. Wiley & Sons, 2004.
23. Law, A. M.; Kelton, W. D. *Simulation Modeling and Analysis*; Third edition, Boston, MA: McGraw –Hill, 2000, pp. 363.
24. Schweizer, S. M.; Moura, J.M.F. Hyperspectral imagery: clutter adaptation in anomaly detection. *IEEE Trans. Information Theory* **August 2000**, *46* (5), 1855–1871.
25. Lehmann, E. L. *Testing Statistical Hypotheses*; New York: transferred to Chapman & Hall, 2nd Edition, 1993.
26. Stocker, A.; Reed, I. S.; Yu, X. Multidimensional signal processing for electro-optical target detection. *Proc. SPIE*, Orlando, FL, vol. 1035, April 1990.
27. Margalit, A.; Reed, I. S. Adaptive detection of stationary optical and IR targets using correlated scene. Ph.D dissertation, Univ. of Southern Calif., Los Angeles, November 1984.
28. Vapnik, V. N. *The Nature of Statistical Learning Theory*; Springer, 1995.
29. Baudat, G.; Anouar, F. Generalized discriminant analysis using a kernel approach. *Neural Computation* **2000**, *12*, 2385–2404.

30. Qin, J.; Zhang, B. A goodness of fit test for logistic regression models based on case-control data. *Biometrika* **1997**, *84*, 609–618.
31. Fokianos, K.; Kedem, B.; Qin, J. A semiparametric approach to the one-way layout. *Technometrics* **2001**, *56*–65.
32. Scheffe, H. *The Analysis of Variance*; New York: John Wiley & Sons, 1959, Chapter 3.
33. Rosario, D.; Rauss, P. Experimental Results Detecting Camouflaged Soldiers in VNIR Hyperspectral Imagery in *Proceedings of the 2005 Military Sensing Symposia (MSS)*, 14–18 February 2005.

Acronyms

ACBC	autonomous clutter background characterization
ARDEC	Armament Research, Development, and Engineering Center
ARL	U.S. Army Research Laboratory
AVT	Asymmetric Variance Test
GV	ground view
HS	hyperspectral
PRS	parallel random sampling
PRS-AVT	PRS using the AVT detector
PRS-RX	PRS using the RX detector
RX	Reed-Xiaoli
SOC	Surface Optics Corporation
STD or sigma	standard deviation
VNIR	visible to near infrared

<u>No. of Copies</u>	<u>Organization</u>	<u>No. of Copies</u>	<u>Organization</u>
1 (PDF)	ADMNSTR ONLY) DEFNS TECHL INFO CTR ATTN DTIC OCP 8725 JOHN J KINGMAN RD STE 0944 FT BELVOIR VA 22060-6218	1 HC	US MILITARY ACDMY MATHEMATICAL SCI CTR OF EXCELLENCE ATTN MAJ J HARTKE PHOTONICS CENTER WEST POINT NY 10996-1786
2 HCs	DARPA ATTN F PATTEN ATTN IXO S WELBY 3701 N FAIRFAX DR ARLINGTON VA 22203-1714	1 HC	PM TIMS, PROFILER (MMS-P) AN/TMQ-52 ATTN B GRIFFIES BUILDING 563 FT MONMOUTH NJ 07703
1 HC	NGA ATTN R S RAND 12310 SURSISE VALLEY DR MAIL STOP DN 11 RESTON VA 20191-3449	1 HC	US ARMY ABERDEEN TEST CENTER ATTN CSTE DT AT WC A F CARLEN 400 COLLERAN ROAD APG MD 21005-5009
1 CD	OFC OF THE SECY OF DEFNS ATTN ODDRE (R&AT) THE PENTAGON WASHINGTON DC 20301-3080	1 HC	US ARMY ABERDEEN TEST CENTER ATTN CSTE DTC AT TC N D L JENNINGS 400 COLLERAN ROAD APG MD 21005-5059
1 HC	US ARMY RSRCH DEV AND ENGRG CMND ARMAMENT RSRCH DEV AND ENGRG CTR ARMAMENT ENGRG AND TECHNLGY CTR ATTN AMSRD AAR AEF T J MATTES BLDG 305 APG MD 21005-5001	1 HC	US ARMY ERDC ATTN CEERD TR S 7701 TELEGRAPH RD BLDG 2592 ALEXANDRIA VA 22315
2 HCs	US ARMY TRADOC BATTLE LAB INTEGRATION & TECHL DIRCTR ATTN ATCD B ATTN ATCH B 10 WHISTLER LANE FT MONROE VA 23651-5850	1 HC	US ARMY INFO SYS ENGRG CMND ATTN AMSEL IE TD F JENIA FT HUACHUCA AZ 85613-5300
1 HC	CDR US ARMY TACOM ARDEC ATTN AMSRD AAR AEP S PAUL GRANGER BLDG 94 PICATINNY ARSENAL NJ 0706-5000	3 HCs	US ARMY MATERIEL SYS ANAL ACTVTY ATTN AMSRD AMS SC G KISTNER ATTN AMSRD AMS SC J MAZZ ATTN AMSRD AMS SC R WHEELER 392 HOPKINS RD APG MD 21005-5071
		1 HC	US ARMY NATICK RDEC ACTING TECHL DIR ATTN SBCN TP P BRANDLER KANSAS STREET BLDG 78 NATICK MA 01760-5056

<u>No. of Copies</u>	<u>Organization</u>	<u>No. of Copies</u>	<u>Organization</u>
1 HC	US ARMY PM NV/RSTA ATTN SFAE IEW&S NV 10221 BURBECK RD FT BELVOIR VA 22060-5806	4 HCs	US ARMY RDECOM CERDEC NVESD ATTN AMSRD CER NV OD J RATCHES ATTN AMSRD CER NV SPPD IST H KLING ATTN AMSRD CER NV SPPD IST S DUNBAR ATTN AMSRD CER NV ST J HILGER 10221 BURBECK RD STE 430 FT BELVOIR VA 22060-5806
1 HC	COMMANDER US ARMY RDECOM ATTN AMSRD AMR W C MCCORKLE 5400 FOWLER RD REDSTONE ARSENAL AL 35898-5000	1 HC	US ARMY RDECOM TARDEC ATTN AMSRD TAR R G R GERHART 6501 E ELEVEN RD MS 263 WARREN MI 48397-5000
2 HCs	US ARMY RDECOM AMRDEC ATTN AMSRD AMR SG IP H F ANDERSON ATTN AMSRD AMR SG W PITTMAN BLDG 5400 REDSTONE ARSENAL AL 35809	4 HCs	DIRECTOR US ARMY RSRCH LAB ATTN AMSRD ARL RO EL L DAI ATTN AMSRD ARL RO M D ARNEY ATTN AMSRD ARL RO MI R ZACHERY ATTN AMSRD ARL RO MM M-H CHANG PO BOX 12211 RESEARCH TRIANGLE PARK NC 27709-2211
1 HC	US ARMY RDECOM AMRDEC ATTN AMSRD AMR SG IR R SIMS BLDG 5400 REDSTONE ARSENAL AL 35898	1 HC	US ARMY SOLDIER & BIOLOGICAL CHEM CTR ATTN AMSRD ECB RT DE W LOEROP EDGEWOOD CHEM & BIOLOGICAL CTR BLDG E-5554 APG MD 21010-5424
1 HC	US ARMY RDECOM ARDEC ATTN AMSRD AAR AER BILL SMITH BLDG 94 PICATINNY ARSENAL NJ 07806-5000	1 HC	COMMANDER USAISEC ATTN AMSEL TD BLAU BUILDING 61801 FT HUACHUCA AZ 85613-5300
1 HC	US ARMY RDECOM ARDEC ATTN AMSRD AAR MEF S JOAO ROMANO BLDG 704 PICATINNY ARSENAL NJ 07806-5000	1 HC	US GOVERNMENT PRINT OFF DEPOSITORY RECEIVING SECTION ATTN MAIL STOP IDAD J TATE 732 NORTH CAPITOL ST NW WASHINGTON DC 20402

<u>No. of Copies</u>	<u>Organization</u>	<u>No. of Copies</u>	<u>Organization</u>
3 HCs	SITAC ATTN H STILES ATTN K WHITE ATTN R DOWNE 11981 LEE JACKSON MEMORIAL HWY STE 500 FAIRFAX VA 22033-3309	18 HCs	US ARMY RSRCH LAB ATTN AMSRD ARL CI ES A WETMORE ATTN AMSRD ARL CI ES K GURTON ATTN AMSRD ARL CI OK PE TECHL PUB ATTN AMSRD ARL CI OK TL TECHL LIB ATTN AMSRD ARL SE E P GILLESPIE ATTN AMSRD ARL SE EE N GUPTA ATTN AMSRD ARL SE EE S KENNERLY ATTN AMSRD ARL SE J PELLEGRINO ATTN AMSRD ARL SE S J EICKE ATTN AMSRD ARL SE SE D ROSARIO (6 copies) ATTN AMSRD ARL SE SE N NASRABADI ATTN AMSRD ARL SE SE N SROUR ATTN IMNE ALC IMS MAIL & RECORDS MGMT ADELPHI MD 20783-1197
1 HC	US ARMY RSRCH LAB ATTN AMSRD ARL CI OK TP TECHL LIB T LANDFRIED BLDG 4600 APG MD 21005-5066		
1 HC	US ARMY RSRCH LAB ATTN AMSRD ARL WM BF G HAAS APG MD 21005-5066		
1 HC	US ARMY RSRCH LAB ATTN AMSRD ARL WM BF W OBERLE BLDG 390 APG MD 21005-5066		
1 HC	DIRECTOR US ARMY RSRCH LAB ATTN AMSRD ARL RO EV W D BACH PO BOX 12211 RESEARCH TRIANGLE PARK NC 27709	Total:	64 (1 PDF, 1 CD, 62 HCs)